Spectral decomposition of internal gravity wave sea surface height in global models

Anna C. Savage,[1] Brian K. Arbic,[2] Matthew H. Alford,[3] Joseph K. Ansong,[2] J. Thomas Farrar,[4] Dimitris Menemenlis,[5] Amanda K. O'Rourke,[2] James G. Richman,[6] Jay F. Shriver,[7] Gunnar Voet,[3] Alan J. Wallcraft,[7] Luis Zamudio[6]

Corresponding author: A. C. Savage, Applied Physics Program, University of Michigan, Ann Arbor, MI 48109, USA. (savagea@umich.edu)

[1]Applied Physics Program, University of

Abstract.

Michigan, Ann Arbor, Michigan, USA

[2]Department of Earth and Environmental Sciences, University of Michigan, Ann Arbor, Michigan, USA

[3]Scripps Institution of Oceanography, University of California, San Diego, La Jolla California, USA

[4]Physical Oceanography Department, Woods Hole Oceanographic Institution, Woods Hole, MA, USA

[5]Earth Sciences Division, Jet Propulsion Laboratory, California Institute of Technology, Pasadena, CA, USA

[6]Center for Oceanic-Atmospheric Prediction Studies, Florida State University, Tallahassee, Florida, USA

[7]Oceanography Division, Naval Research Laboratory, Stennis Space Center, Mississippi, USA

Two global ocean models ranging in horizontal resolution from 1/12° to 1/48° are used to study the space- and time-scales of sea surface height (SSH) signals associated with internal gravity waves (IGWs). Frequency-horizontal wavenumber SSH spectral densities are computed over seven regions of the world ocean from three simulations of the HYbrid Coordinate Ocean Model (HYCOM) and two simulations of the Massachusetts Institute of Technology general circulation model (MITgcm). High-wavenumber, high-frequency SSH variance follows the predicted IGW linear dispersion curves. The realism of high-frequency motions (> 0.87 cpd) in the models is tested through comparison of the frequency spectral density of dynamic height variance computed from the highest resolution runs of each model (1/25° HYCOM and 1/48° MITgcm) with dynamic height variance frequency spectral density computed from 9 in-situ profiling instruments. These high-frequency motions are of particular interest because of their contributions to the small-scale SSH variability that will be observed on a global scale in the upcoming Surface Water and Ocean Topography (SWOT) satellite altimetry mission. The variance at supertidal frequencies can be comparable to the tidal and low-frequency variance for high-wavenumbers (length scales smaller than $\sim$ 50 km), especially in the higher resolution simulations. In the highest resolution simulations, the high-frequency variance can be greater than the low-frequency variance at these scales.

1. Introduction

Satellite altimetry has enabled global-scale calculations of sea surface height (SSH) wavenumber spectral density whose slope has been used to diagnose low-frequency dynamics of the ocean surface [*Stammer*, 1997; *Le Traon et al.*, 2008; *Sasaki and Klein*, 2012; *Xu and Fu*, 2012; *Richman et al.*, 2012]. Two-dimensional swath altimetry, as in the upcoming Surface Water and Ocean Topography (SWOT) satellite mission, will sample SSH along two-dimensional swaths [*Fu et al.*, 2012]. In SWOT, these swaths will measure 100 km wide with 1 km x 1 km pixels and will have a repeat cycle of $\sim$ 21 days. This dataset will provide a new opportunity to compute SSH wavenumber spectral density from two-dimensional observed data [*Fu et al.*, 2012]. As with previous altimeter missions, SWOT will suffer from infrequent temporal sampling and will therefore alias the SSH signatures of high-frequency motions, such as internal tides and the internal gravity wave (IGW) continuum. The aliasing of such motions contaminates low-frequency signals in altimeter data [*Ray and Byrne*, 2010; *Shriver et al.*, 2012; *Ray and Zaron*, 2016].

The IGW continuum [*Garrett and Munk*, 1972] is thought to arise from nonlinear interactions between near-inertial waves driven by wind [*D'Asaro*, 1984] and internal tides generated by barotropic tidal flow over rough topography [*Ray and Mitchum*, 1997]. Aside from their implications for satellite altimetry, IGWs are of interest due to the control they exert over deep ocean mixing, and hence, the oceanic meridional overturning circulation [*Munk and Wunsch*, 1998; *Ferrari and Wunsch*, 2009]. The rich spatial pattern of oceanic mixing has recently been revealed by finestructure methods applied to ARGO floats [*Whalen et al.*, 2012]. Recently, high-resolution ocean models forced by both atmo-

spheric fields and tides [*Arbic et al.*, 2010, 2012] have been shown to partially resolve the IGW continuum [*Müller et al.*, 2015]. *Müller et al.* [2015] examined frequency-horizontal wavenumber spectral density of IGW kinetic energy over one North Pacific region in two high-resolution simulations of the HYbrid Coordinate Ocean Model [HYCOM; *Chassignet et al.*, 2009]. Here, we build upon results in *Müller et al.* [2015] by examining SSH spectral density in seven regions, in both HYCOM and the Massachussets Institute of Technology general circulation model [MITgcm; *Marshall et al.*, 1997] simulations forced simultaneously by atmospheric fields and tides. We aim to quantify some of the differences between the HYCOM and MITgcm simulations, particularly at high frequencies and wavenumbers, where global ocean models are only beginning to perform. In addition, we aim to estimate the contributions of different frequency bands to the small-scale dynamics of interest for the SWOT mission.

To check high-frequency motions in the models against in-situ data, dynamic height variance frequency spectral densities are computed in HYCOM and MITgcm at 9 locations where high-frequency and high-vertical resolution in-situ McLane profiler [*Doherty et al.*, 1999] salinity and temperature data are available for comparison [*Zantopp and Leaman*, 1984; *Savage et al.*, 2017]. Dynamic height arises from baroclinic motions [*Baker-Yeboah et al.*, 2009], such as fronts, eddies, and internal gravity waves. High-frequency dynamic height signals include diurnal and semidiurnal internal tides [*Shriver et al.*, 2012; *Ray and Zaron*, 2016; *Zhao et al.*, 2016], as well as supertidal motions, which can be attributed to the IGW continuum [*Glazman and Cheng*, 1999].

After comparing both models against in-situ observations, we use hourly SSH fields from two simulations of HYCOM and three simulations of MITgcm of varying horizontal

resolution to compute frequency-horizontal wavenumber spectral density in seven regions. The seven regions were chosen to exemplify areas dominated by different ocean dynamics, e.g. internal tides and gravity waves versus mesoscale eddies. As in *Müller et al.* [2015], we show that large variance exists along the linear dispersion curves for the three gravest vertical modes, indicating partial resolution of the IGW continuum. We also examine the impact of horizontal resolution on the ability of models to simulate the IGW continuum [*Müller et al.*, 2015].

To study the contributions of different frequency bands to SSH variance wavenumber spectral density, we integrate the frequency-horizontal wavenumber spectral densities over three frequency bands of interest: subtidal, tidal, and supertidal. We examine whether high-frequency motions can dominate at high-wavenumbers, as has been done in earlier studies [*Richman et al.*, 2012; *Callies and Ferrari*, 2013; *Rocha et al.*, 2016a], and whether the strength of high-frequency motions increases with increased horizontal resolution of the models.

2. Observations and models

2.1. McLane profilers

The locations of the 9 McLane profilers [*Doherty et al.*, 1999] used in this study are given in Table 1. The profilers are clustered in three regions in the Pacific: profilers a-d are located in the central North Pacific near Hawai'i [*Alford et al.*, 2007; *Zhao et al.*, 2010; *MacKinnon et al.*, 2013a, b], profilers e and f are located in the Luzon Strait [*Alford et al.*, 2011], and profilers g-i are located off of the Oregon coast [*Nash et al.*, 2007; *Martini et al.*, 2011, 2013]. The McLane profilers travel vertically at $\sim$ 25-33 cm/s, and sample temperature and salinity coincidentally throughout the profile. The McLane profiler data

is then interpolated in depth and time to even 2 db vertical intervals and hourly time intervals. Table 1 gives the maximum and minimum pressures used in this study from each instrument. For each instrument, the pressure intervals were chosen so that there were no missing data over the duration of the record. Only profilers in water deeper than 1 km were chosen, as high-frequency dynamic height in shallow water is not necessarily a good representation of internal tides and the IGW continuum. The dynamic height is computed at each hourly time step. Record durations range in length from approximately 22-51 days, and are given in Table 1.

2.2. HYCOM simulations

General information about HYCOM can be found in *Chassignet et al.* [2009]. Two simulations of HYCOM are used in this study: one with a 1/12.5° horizontal resolution (HYCOM12; ~ 8 km), the other with a 1/25° horizontal resolution (HYCOM25; ~ 4 km). Both simulations have 41 hybrid vertical layers. The atmospheric fields, including atmospheric pressure, buoyancy, and wind forcing, used in both HYCOM simulations are taken from the U.S. Navy Global Environmental Model, NAVGEM [*Hogan et al.*, 2014]. HYCOM25 is forced by NAVGEM every three hours while HYCOM12 is forced hourly. The HYCOM simulations are forced using a 0.5° application grid interpolated from NAVGEM's primary 37 km grid. The HYCOM simulations are simultaneously forced by the astronomical tidal potential [*Cartwright*, 1999] of the two largest diurnal constituents (K_1 and O_1) and the three largest semidiurnal constituents (M_2, S_2, and N_2). The five tidal constituents used in the HYCOM simulations account for $\sim 97\%$ of the global variance in the ten largest tidal constituents in the Global Ocean Tide Model (GOT99.2; *Ray* [1999]). A Smagorinski scheme is used for vertical viscosity and a Laplacian scheme is used for

horizontal diffusivity, while a KPP scheme is used for vertical diffusivity and viscosity. The self-attraction and loading (SAL, *Hendershott* [1972]) term is computed iteratively as described in *Buijsman et al.* [2015]. A topographic wave drag field taken from *Jayne and St. Laurent* [2001] is tuned to minimize barotropic tidal errors with respect to the altimeter-constrained tide model TPXO [*Egbert et al.*, 1994]. The same wave drag tuning computed for HYCOM12 was used for HYCOM25. A description of the wave drag tuning can be found in *Buijsman et al.* [2015], and more information on the importance of the wave drag on barotropic and baroclinic tides can be found in *Ansong et al.* [2015] and *Buijsman et al.* [2016]. An Augmented State Ensemble Kalman Filter is implemented in both simulations to reduce the global RMS error of M_2 barotropic tidal elevations in waters deeper than 1 km, with respect to TPXO, to approximately 2.6 cm [*Ngodock et al.*, 2016]. The HYCOM output is saved hourly for one full year, yielding $\sim$ 1 TB of SSH fields for HYCOM25. HYCOM12 output spans October 2011 through September 2012, while HYCOM25 output spans January 2014 through December 2014.

Several model-data comparisons have been performed with the HYCOM tidal simulations, including comparison of barotropic and internal tide SSH signatures to altimetry [*Shriver et al.*, 2012; *Stammer et al.*, 2014; *Ansong et al.*, 2015; *Ngodock et al.*, 2016], comparison of surface tidal elevations to pelagic [*Stammer et al.*, 2014] and coastal [*Savage et al.*, 2017] tide gauges, comparison of tidal currents to moored current meter records [*Timko et al.*, 2012, 2013; *Stammer et al.*, 2014], comparison of IGW kinetic energy frequency spectral densities to current meter spectral densities [*Müller et al.*, 2015], comparison of baroclinic tidal energy fluxes to fluxes computed from current meter records [*Ansong et al.*, 2017], and a previous comparison of dynamic height variance frequency

spectral densities with in-situ depth profiling instruments [*Savage et al.*, 2017]. In general, these studies have shown that HYCOM well represents internal tides, but is too weak in supertidal frequencies. Additionally, due to topographic wave drag, tides in HYCOM are often less energetic than in other similar models.

2.3. MITgcm simulations

Three global ocean simulations of MITgcm [*Marshall et al.*, 1997] are used in this study: one with 1/12° (3-9 km) horizontal grid spacing (hereinafter MITgcm12), one with 1/24° (2-5 km) grid spacing (MITgcm24), and one with 1/48° (.75-2.3 km) grid spacing (MITgcm48). All three simulations have 90 z-levels in the vertical direction with thicknesses ranging from 1 m at the surface to 480 m near the bottom at a maximum model depth of 7 km. Bathymetry is from *Smith and Sandwell* [1997] Version 14.1 and IBCAO Version 2.23 [*Jakobsson et al.*, 2008]. The model is forced at the surface with six-hourly atmospheric fields from the 0.14° European Center for Medium-Range Weather Forecasts (ECMWF) atmospheric operational model analysis, which, starting in 2011, is converted to surface fluxes using the bulk formulae of *Large and Yeager* [2004]. Over ice-covered regions, ocean surface fluxes are computed using the sea ice model of *Losch et al.* [2010]. The model includes atmospheric pressure forcing and tidal forcing for 16 tidal constituents, the latter applied to MITgcm as additional atmospheric pressure forcing [*Ponte et al.*, 2015]. The 16 tidal constituents are made up of 8 long-period tides, (M_t, M_f, M_m, M_{sm}, M_{sf}, S_{sa}, S_s, and L_n) and the 8 largest diurnal (K_1, O_1, P_1, and Q_1) and semidiurnal (M_2, S_2, N_2, and K_2) tidal constituents. A Leith scheme is used for horizontal diffusivity and a KPP scheme is used for vertical diffusivity. The MITgcm12 simulation is initialized on January 1, 2010 from a data constrained 1/6° simulation provided by the Estimating the Circula-

tion and Climate of the Ocean, Phase II (ECCO2) project [*Menemenlis et al.*, 2008] and integrated for one year without tides with ERA-Interim [*Dee et al.*, 2011] surface boundary conditions. The application of tidal forcing and atmospheric boundary conditions from the 0.14° ECMWF analysis starts on January 1, 2011. The MITgcm24 simulation is initialized from MITgcm12 fields on January 17, 2011. The MITgcm48 simulation is initialized from MITgcm24 fields on September 10, 2011. In this study, we use 90 days of hourly model output from the three MITgcm simulations for the following periods: March 1, 2014 through May 29, 2014 for MITgcm12 and October 31, 2011 through January 28, 2012 for MITgcm24 and MITgcm48. The horizontal resolution and record times for each HYCOM and MITgcm simulation are listed in Table 2 for reference.

The MITgcm tidal simulations are newer than the HYCOM tidal simulations, and have received less vetting. The accuracy of the barotropic and internal tides has not yet been tested on a global scale. The MITgcm tidal simulations do not contain wave drag, which was shown in *Ansong et al.* [2015] to be a critical control on globally averaged internal tide amplitudes. Published model-data comparisons to date are limited to a Drake Passage study [*Rocha et al.*, 2016a], that compared along-track wavenumber spectra of kinetic energy in MITgcm48 with Acoustic Doppler Current Profiler data, and a Kuroshio Extension study [*Rocha et al.*, 2016b], that established that the upper ocean stratification and variability in that region is well captured by both the MITgcm24 and MITgcm48 simulations.

3. Methodology

3.1. Model/observation comparison of dynamic height variance

The comparison of modeled versus observed dynamic height variance is done using methods similar to those used in Section 3.2 of *Savage et al.* [2017]. However, whereas *Savage et al.* [2017] integrated the model results from the maximum pressure of the profiling instrument to the surface to estimate modeled steric SSH, here we integrate both the models and observations over the pressure intervals covered by the McLane profilers, yielding an improved model-data comparison. Dynamic height, $h(p_1, p_2)$, is computed as an integral of the specific volume, α, using the standard definition [*Knauss*, 1997] given as

$$h(p_1, p_2) = \frac{1}{g} \int_{p_1}^{p_2} \alpha(S, T, p) dp. \tag{1}$$

The specific volume, $\alpha(S, T, p)$, is defined as $1/\rho(S, T, p)$ where ρ is density and S, T, and p denote salinity, temperature, and pressure, respectively. The factor of $1/g$ accounts for gravity, and we solve for height, $h(p_1, p_2)$, where p_1 and p_2 are the minimum and maximum pressure levels over which we perform the integration. A trapezoidal integration technique is used in Equation (1). Before integration, HYCOM25 temperature and salinity are interpolated onto even 50 db pressure intervals, as the large pressure intervals in the deep ocean in HYCOM output do not provide the vertical resolution necessary for computation of dynamic height. Figure 1 displays time-pressure series of density anomaly profiles from one of the profilers off the Oregon coast in (a) the McLane profiler, (b) HYCOM25, and (c) MITgcm48. The average number of pressure levels used to compute dynamic height is $\sim$ 630 in the McLane profilers, $\sim$ 26 in HYCOM25, and $\sim$ 36 in MITgcm48.

Over the pressure intervals shown in the figure, the model profiles of density anomaly appear similar to the McLane profiles, with MITgcm48 appearing more negative than the McLane profiler or HYCOM25 near the top of the water column in the latter half of the record shown. The records shown are taken from the first 200 hours of each dataset, and therefore do not span the same time intervals. The McLane profiler data was collected beginning in September, the HYCOM25 data shown is from January, and the MITgcm48 data shown begins in October (Tables 1 and 2). Time series of dynamic height anomaly about the time mean are shown in (Figure 1d) McLane Profiler, (1e) HYCOM25, and (1f) MITgcm48. The variabilities in the three time series span $\sim 4\,\mathrm{cm}$, but while the HYCOM25 time series of dynamic height (Figure 1e) appears to oscillate smoothly with the semidiurnal signal, both the McLane profiler and the MITgcm48 time series appear to have higher frequency signals in addition to the semidiurnal signal.

Following computation of dynamic height time series, frequency spectral densities are computed. Both a linear trend and mean are removed from each time series. The dynamic height time series are then multiplied by a Tukey window having a taper-to-constant ratio of 0.2. The Tukey window removes approximately $15 - 20\%$ of the variance from the spectral densities. The frequency spectral densities are computed for each one year HYCOM25 time series, each three month MITgcm48 time series, and each McLane profiler time series, with the latter having varying record lengths. A discrete Fourier Transform is used, given by

$$\hat{h}_m(\omega_m) = \sum_{n=0}^{N-1} h_n e^{\frac{-2\pi i m n}{N}}, \tag{2}$$

where ω denotes frequency, m and n are indices for the Fourier series and physical series, respectively, and N is the total number of samples. The 95% confidence intervals are computed and account only for random error in spectral density calculations. The confidence intervals are calculated by averaging the spectral density values with neighboring points. As the frequency axis is logarithmic, the averaging window is small at low-frequencies and larger at high-frequencies. Thus, the confidence intervals are narrower at high-frequencies than at low-frequencies. The width of the averaging window ranges from 3 points at low-frequencies for both models and observations to 21 points at high-frequencies for the McLane profiler data and 50 points at high-frequencies for both models. The variance in three frequency bands—the diurnal [frequencies between 0.87 cpd and 1.05 cpd], the semidiurnal [frequencies between 1.86 cpd and 2.05 cpd] and the supertidal [frequencies greater than 2.06 cpd]—are computed by summing over the unsmoothed periodogram, $|\widehat{h}(\omega)|^2$ as

$$h^2 = \frac{2}{N^2} \sum_{m=a/2}^{b/2} |\hat{h}_m(\omega_m)|^2, \tag{3}$$

where a and b are indices such that ω_a and ω_b are the limiting frequencies, defined above.

3.2. Frequency-horizontal wavenumber spectral density

Frequency-horizontal wavenumber spectral densities of SSH are computed from the HYCOM and MITgcm simulations over seven regions. The locations and bathymetries of the seven regions are displayed in Figure 2a and the HYCOM25 subtidal SSH variance in each region is shown in Figure 2b. The longitudinal and latitudinal ranges of each region are listed in Table 3, along with abbreviations for each region used in several figures. Three-month blocks of hourly data were used from all five simulations. The

three-month time period is dictated by the amount of data available from the highest resolution model, MITgcm48, at the time of output collection. The first three months of the records listed in Table 2 for HYCOM12 and HYCOM25 were used to computed frequency-horizontal wavenumber spectral densities. Before the spectral densities are computed, the temporal and two-dimensional spatial trends and means are removed and a Tukey window having a taper-to-constant ratio of 0.2 is employed in time and along both spatial dimensions. Frequency-horizontal wavenumber spectral density is computed via a discrete three-dimensional Fourier Transform, given as

$$\hat{\eta}_{p,h,m}(k_p, l_h, \omega_m) = \sum_{q=0}^{Q-1} \sum_{g=0}^{G-1} \sum_{n=0}^{N-1} \eta_{q,g,n} e^{-2\pi i(\frac{pq}{Q} + \frac{hg}{G} + \frac{mn}{N})}, \tag{4}$$

where η denotes sea surface height, ω denotes frequency, k denotes zonal wavenumber, and l denotes meridional wavenumber. Indices p, h, and m are for the Fourier series, and q, g, and n are indices for the physical series. The total number of samples in the zonal, meridional, and temporal directions are denoted as Q, G, and N, respectively.

The three-dimensional Fourier transform in (4) is used to compute a two-dimensional spectral density, $|\hat{\eta}(K, \omega)|^2$, along isotropic (radial) wavenumber, K [*Lumley*, 1970]. The isotropic wavenumber vector, K, is defined here as an evenly distributed discrete set of wavenumbers whose length is arbitrarily chosen to equal the artithmetic mean of the lengths of k and l. The minimum and maximum values of the vector K are the minimum and maximum values of $\sqrt{k^2 + l^2}$, respectively. The spectral density contribution to the r^{th} element of isotropic wavenumber, K_r, can be computed as

$$|\hat{\eta}_r(K_r,\omega)|^2 = \begin{cases} \frac{2}{QGN}\left[\sum_{p=1}^{\chi}\sum_{h=1}^{\zeta}|\hat{\eta}_{p,h}(k_p,l_h,\omega)|^2\right], & \text{if } r=1 \\ \frac{2}{QGN}\left[\sum_{p=1}^{\chi}\sum_{h=1}^{\zeta}|\hat{\eta}_{p,h}(k_p,l_h,\omega)|^2\right] - \sum_{\gamma=1}^{r-1}|\hat{\eta}_{\gamma}(K_{\gamma},\omega)|^2, & \text{if } r>1 \end{cases} \quad (5)$$

where $k_\chi^2 + l_\zeta^2 < K_r^2$, and r is an index which spans 1 to the length of K. This definition of $|\hat{\eta}(K,\omega)|^2$ is computed iteratively. The first term on the right hand side of Equation (5) is a sum over all values of $|\hat{\eta}(k,l,\omega)|^2$ for which k and l satisfy the condition $k_\chi^2 + l_\zeta^2 < K_r^2$, and the second term on the right hand side in the condition that $r > 1$ is a sum over all previously computed values of $|\hat{\eta}(K,\omega)|^2$. This method conserves variance when transforming from anisotropic to isotropic spectral density.

Internal gravity wave linear dispersion relation curves are computed by solving for the eigenspeeds [*Munk*, 1981] using the Sturm-Liouville equation for vertical modes. The Sturm-Liouville problem that we solved makes standard assumptions, i.e. a constant Coriolis parameter f, a buoyancy frequency N^2 that depends on latitude and the vertical coordinate z, and a constant seafloor depth H. As in *Müller et al.* [2015], we use the extreme eigenspeed values, computed for local values of f, N^2, and H for each grid point on the northern and southern boundaries of a region, in order to ascertain bounding dispersion curves. Although both models are hydrostatic, the Sturm-Liouville equation that we solve uses a non-hydrostatic vertical momentum equation. The differences that may arise from this discrepancy would most prominently affect frequencies near the buoyancy frequency, and would not greatly affect the frequencies of interest in this study. Because the eigenspeeds are greatly dependent on water column depth, H, the extreme eigenspeeds were chosen from grid points with $H > 1\,\text{km}$. The assumption of a relatively constant bottom depth H is only really valid in the North Pacific region (Figure 2a). While it is difficult to find large regions in the ocean that have nearly constant bottom depth, we

note that grid points with depths shallower than 500 m comprise less than 0.5% of the grid points in each of the seven regions used for this study. The validity of frequency-horizontal wavenumber spectral densities also hinges on horizontal homogeneity of the fields. Figure 2b shows the HYCOM25 subtidal SSH variance (computed as in *Savage et al.* [2017]) in the boxes used in this study. While the majority of our boxes are horizontally homogeneous, the Kuroshio and especially the North Atlantic regions have areas of large subtidal variance that changes rapidly in space. However, we find that this horizontal inhomogeneity of low-frequency motions does not significantly affect the IGW modes of main interest in this study, as the supertidal SSH variance is relatively homogeneous (see Figure 16 in *Savage et al.* [2017]). We also note that the desire for large horizontal regions with relatively constant bottom depth prohibits our ability to calculate frequency-horizontal wavenumber spectral density in regions colocated with our in-situ data in the Luzon Strait and off of the Oregon coast.

4. Results

4.1. Model/observation comparison

Dynamic height variance frequency spectral density comparisons between HYCOM25, MITgcm48, and the 9 McLane profilers are shown in Figure 3. The order of the subplots corresponds to the order of profilers in Table 1. At low frequencies, ($\omega \leq 0.2\,\mathrm{cpd}$), both models agree with data in five of the nine locations. Large peaks are seen at semidiurnal frequencies at six of the nine locations, indicative of large semidiurnal internal tides. Additionally, large peaks are seen at diurnal frequencies in Figures 3e and 3f, representing the Luzon Strait where diurnal internal tides are known to be large [*Jan et al.*, 2008]. Diurnal peaks are also clear in Figures 3h and 3i, off the Oregon coast, where the strength

of diurnal tides is known to be highly variable [*Erofeeva et al.*, 2003]. In the Hawai'i cluster (Figures 3a-3d) as well as Figure 3g (Oregon coast), both models are deficient compared to data at frequencies ranging from $\sim 0.2\,\mathrm{cpd} - 1\,\mathrm{cpd}$, for reasons that are not clear but may have to do with the inability of the models to represent fast submesoscale motions. In most locations, MITgcm48 matches the observations better than HYCOM25 does in supertidal frequencies ($\omega > 2.06\,\mathrm{cpd}$), consistent with *Savage et al.* [2017], that showed that HYCOM25 SSH is deficient compared to observations at supertidal frequencies.

This low bias of HYCOM25 at supertidal frequencies is confirmed in Table 4, that lists the standard deviation (computed as the square root of the band-integrated variance [Equation 3]) at all nine locations. The model performances are similar in the diurnal and semidiurnal tidal ranges. However, in the supertidal band, MITgcm48 is substantially closer to the McLane observations than HYCOM25 is, in five of the nine locations. Figure 4 shows the band-integrated variance (the squares of standard deviations listed in Table 4) in the form of scatter plots. In diurnal and semidiurnal bands (Figures 4a and 4b), variance estimates from HYCOM25 and MITgcm48 agree with observations with respect to the 1-to-1 (black dashed) lines. Additionally, the variance estimates from both models are near equal at all locations. In Figure 4c, the supertidal band, HYCOM25 is biased low compared to the 1-to-1 line, particularly at locations g-i, the profilers located off the Oregon coast. This deficiency in HYCOM25 may be due to the lower horizontal and vertical resolution of HYCOM25 relative to MITgcm48. It has been shown that model horizontal resolution affects the strength of the IGW continuum [*Müller et al.*, 2015; *Savage et al.*, 2017]. Another possible source of discrepancy between the model estimates of supertidal variance is the lack of wave drag parametrization in MITgcm, that would tend

to yield strong high-frequency motions in MITgcm relative to HYCOM. As there are only nine McLane profilers that provide the high vertical resolution and high-frequency data necessary for calculation of dynamic height, this model/observation comparison offers limited insight into which model, if either, is accurately representing oceanic high-frequency dynamics. While MITgcm certainly appears to be outperforming HYCOM in these nine locations, we cannot say that this is representative of model performance on a global scale.

4.2. Frequency-horizontal wavenumber spectral density of SSH

Sea surface height variance frequency-horizontal wavenumber spectral densities, computed from MITgcm48 over all seven regions shown in Figure 2, are displayed in Figure 5. Similar collections of frequency-horizontal wavenumber spectral densities computed from HYCOM12, HYCOM25, MITgcm12, and MITgcm24 in all seven regions are given in the supplementary material. To allow for easier comparison across simulations, the wavenumber axis in all subplots of Figure 5, and in the corresponding supplementary figures, is set to the maximum horizontal wavenumber computed for HYCOM25. All of the subplots in Figure 5 show the linear dispersion curves for the first three IGW vertical modes, depicted as white curves. The dispersion curves are computed from the Sturm-Liouville problem at all the model gridpoints (in water deeper than 1 km) along the northern and southern boundaries of the regions. As in *Müller et al.* [2015], maxima and minima of the eigenspeeds are used to draw bounding dispersion curves for each mode in each region. The IGW dispersion relation curves vary greatly between regions. In each region, the areas within the bounding dispersion curves stand out as having larger variance compared to the background, and appear most prominently in the North Pacific (Figure 5a), the Equatorial Pacific (Figure 5d) and the Indian Ocean (Figure 5g), all regions known to

have a large IGW SSH signature [*Savage et al.*, 2017]. The Kuroshio (Figure 5c) and the North Atlantic (Figure 5f) display large variance at low-frequency and low-wavenumber, indicative of regions with strong mesoscale activity. The high variance lying along the dispersion curves in these strongly eddying regions appear more blurred in the wavenumber direction than in some weakly eddying regions, such as the North Pacific, suggesting that the low frequency modulation of IGWs by mesoscale eddies in these regions affects the dynamics of the IGW SSH signatures. The semidiurnal internal tides are prominent (appearing as spots of large variance within the dispersion curves at 2 cpd) in the spectral densities of all regions. These semidiurnal internal tides have larger variance than the background semidiurnal tidal variance (horizontal stripes at 2 cpd) in the Kuroshio (Figure 5c), the Equatorial Pacific (Figure 5d), the North Atlantic (Figure 5f), and the Indian Ocean (Figure 5g). The dispersion curves for the other simulations, shown in the supplementary material, are qualitatively similar to the MITgcm48 plots shown in Figure 5.

SSH variance frequency-horizontal wavenumber spectral densities in the North Pacific region from all five simulations are shown in Figure 6. Increasing horizontal resolution yields a more energetic IGW continuum [*Müller et al.*, 2015]. For instance, the HYCOM25 spectral densities are noticeably more spread out along the dispersion curves than the HYCOM12 spectral densities (Figure 6). Similarly, the MITgcm48 spectral densities are more spread out along the dispersion curves than the MITgcm24 spectral densities, that in turn are more filled out than the MITgcm12 spectral densities. There are large peaks at higher tidal harmonics; however they appear to be less prominent in HYCOM25 than in HYCOM12. Similarly, it appears that the higher harmonics become less prominent

as resolution increases in the MITgcm simulations. We speculate that the prominent higher harmonics arise from a combination of several aspects of our analysis. These large variance horizontal stripes may be artifacts of the lack of resolution of internal wave triads in lower resolution simulations. The higher harmonics become less prominent as resolution increases and models are better able to represent more wave triads, thus filling out the spectrum more completely [*Müller et al.*, 2015].

We also conjecture that these stripes are, to some extent, artifacts of the Tukey window used to enforce periodicity prior to the calculation of the discrete Fourier Transform (Equation 4). Tukey windows, like other rectangular windows, are known to have problems with spectral leakage [*Harris*, 1976]. We choose to use a Tukey window because using a windowing function that minimizes the spectral leakage also removes more of the variability of interest. HYCOM12 and MITgcm12 show similar dynamics, with slightly larger variance along the first mode in MITgcm12. Similarly, MITgcm24 has more variance along the first mode than HYCOM25. In the HYCOM25, MITgcm24, and MITgcm48 spectral densities, the high variance along the dispersion curves folds back after reaching the Nyquist frequency of 12 cpd. This indicates that the hourly sampling is insufficient because, in some regions, there is significant variance in high-frequency motions that are not resolved with one hour sampling. Additionally, the aliasing seems to be strong in the North Pacific (Figure 5a), the Equatorial Pacific (Figure 5d), and the Indian Ocean (Figure 5g), where the IGW signal is known to be large.

4.3. Frequency band contributions to wavenumber spectral density

To quantify the contributions from different frequency bands to the wavenumber spectral density, the frequency-horizontal wavenumber spectral densities (Equation 5) are

integrated over three frequency bands: the subtidal band [$\omega < 0.86\,\mathrm{cpd}$], the tidal band [$0.87 < \omega < 2.05\,\mathrm{cpd}$], and the supertidal band [$\omega > 2.06\,\mathrm{cpd}$]. Due to known impacts of dissipation schemes on the effective resolution of ocean models [*Soufflet et al.*, 2016], a caveat of this study is that we are unable to examine the high-wavenumbers affected by the spectral roll off associated with eddy viscosity. This roll off can be clearly seen at the high-wavenumber [$\sim (3\delta x)^{-1}$] end of the wavenumber spectral densities discussed in this section (Figures 7 and 8). For these reasons, we limit our study to wavenumbers $< (3\delta x)^{-1}$, and the effective resolution limits for each simulation are listed in Table 2. The MITgcm48 wavenumber spectral densities for all seven regions shown in Figure 2 from the three frequency bands of interest are given in Figure 7. The ratio of supertidal variance to total variance is plotted as a purple dashed-dotted line and references the right axes in Figures 7 and 8. Supplementary Figures 5-8 show the wavenumber spectral density contributions in the other four simulations. In all regions, supertidal phenomena contribute very little at low wavenumbers, but are substantial at scales of approximately 100 km and smaller. At scales smaller than $\sim 50\,\mathrm{km}$, either the tidal or supertidal frequency bands dominate in every region. In all regions, the ratio of supertidal variance to total variance shows a sharp increase at $\sim 250\,\mathrm{km}$ where it is a minimum, and increases continuously until it reaches nearly 1 at scales varying by location. The ratio of supertidal to total variance drops off at the highest wavenumbers in the South East Pacific, South Pacific, and Indian Ocean (Figures 7b, 7e, and 7g) and may be related to high wavenumber roll off described above. The two humps prominent in the Equatorial Pacific (Figure 7d) in the tidal and subtidal bands appear to occur at the wavenumbers affected by the aliasing in Figure 5d. This suggests that the energy in these two humps should actually be attributed

to the supertidal frequency band, if the temporal sampling allowed for resolution of higher frequency IGWs. Less prominent humps can be seen in the North Pacific, South Pacific, and Indian Ocean regions, suggesting that this contamination is prevalent in regions of high IGW activity.

The wavenumber spectral densities of subtidal, tidal, and supertidal frequency bands for all five simulations in the Kuroshio region are shown in Figure 8. While the contributions from the three frequency bands of interest at low-wavenumber (scales $\sim 100\,\mathrm{km}$ to $1,000\,\mathrm{km}$) are not strongly sensitive to model horizontal resolution, below these scales, the behavior of the supertidal band changes as horizontal resolution changes. Across all simulations, the subtidal and tidal bands dominate at large scales. The supertidal band appears to dominate in MITgcm24 and MITgcm48 (Figure 8d and 8e) at scales $\sim 50\,\mathrm{km}$ and smaller. The ratio of supertidal variance to total variance has a minimum at scales of $\sim 250\,\mathrm{km}$ in all simulations, and nears one at smaller length scales in the two highest resolution simulations of MITgcm. In both HYCOM simulations, the supertidal contributions only appear to surpass the subtidal and tidal contributions at wavenumbers unlikely to be truly resolved by the model (e.g., in the roll-off regime). Supplementary Figures 5-8 show that the contribution of supertidal variance to total variance differs by region and horizontal resolution, but is always largest at small scales. Additionally, the ratio of supertidal to total variance nears one in the North Pacific, Equatorial Pacific, and Indian Ocean regions, all regions known to have large IGW activity, in HYCOM25, MITgcm24, and MITgcm48. This differs from the results shown in Figure 8, suggesting that away from western boundary currents, the supertidal frequency band dominates at small scales in HYCOM and MITgcm simulations with sufficiently high horizontal resolution. While

Richman et al. [2012] stated that the high-frequency contributions to high-wavenumber spectra were due to internal tides, *Müller et al.* [2015] demonstrated that some HYCOM simulations in fact carried a partial IGW continuum. Here, we have shown that the IGW continuum also contributes to the high-frequency portion of the SSH variance wavenumber spectral density (Figures 5-8), and in some regions dominates in the highest resolution simulations. As in *Qiu et al.* [2017], the length scale at which the supertidal band begins to dominate over the subtidal band was averaged over all simulations in each region, and the length scales are listed in the final column of Table 3. These length scales can be grouped into three categories: (1) highly eddying, high latitude regions (the Kuroshio and North Atlantic regions), (2) low eddying, high latitude regions (the North Pacific, South Pacific, and South East Pacific regions), and (3) low eddying, low latitude regions (the Equatorial Pacific and Indian Ocean regions). The highly eddying, high latitude regions tend towards the smallest transition length scales, whereas the low eddying, low latitude regions tend towards the largest transition length scales. In the regions of high eddy-activity, such as the Kuroshio and the North Atlantic, these transition length scales would be highly dependent on location within the region, and the transition length scales presented here represent an average over the entire region. As with kinetic energy, the transition length scales of SSH are dependent both on latitude and eddy activity [*Qiu et al.*, 2017]. This suggests that the contamination of mesoscale and submesoscale motions in the upcoming SWOT mission will depend on latitude and eddy activity, correlating with the length scales at which supertidal frequencies dominate over the subtidal frequencies.

The differences in the prominence of supertidal motions at small scales with increasing model resolution are more apparent in Figure 9, that plots the same spectral densities as

in Figure 8 but with the subplots separated by frequency band instead of by horizontal resolution. In Figure 9 we therefore see spectral densities at different model resolutions on the same vertical scales. In addition, Figure 9 plots spectral densities for the North Pacific as well as for the Kuroshio. In the subtidal and tidal frequency bands (Figures 9a-9d), the five simulations are relatively well matched at low wavenumbers. The higher resolution simulations display greater high-wavenumber variance in the subtidal and tidal bands in both the North Pacific and Kuroshio regions. In the supertidal band (Figures 9e and 9f), the models show different behaviors in the two regions shown. In the North Pacific, there is a large increase in high-wavenumber variance as horizontal resolution increases in both models (Figure 9e). HYCOM25 has larger variance at these wavenumbers than its resolution counterpart, MITgcm24. However, in the Kuroshio, the increase of high-wavenumber supertidal variance with increased model horizontal resolution is highly pronounced in the MITgcm simulations, and less pronounced in the HYCOM simulations. As the output from HYCOM25 and MITgcm48 was collected from similar times of year, (October-January for MITgcm48 and January-March for HYCOM25), the seasonality of the Kuroshio extension [*Rocha et al.*, 2016b] is unlikely to contribute to this mismatch.

To further examine that the increase in energy with model horizontal resolution, the spectral slopes of the subtidal, tidal, and supertidal wavenumber spectral densities shown in Figures 7-9, and Supplementary Figures 5-8, were computed in all seven regions in all five simulations, and plotted in Figure 10. The slopes were computed over scales ranging from 70-250 km [*Xu and Fu*, 2012; *Richman et al.*, 2012] for the subtidal and tidal bands, and over scales 30-70 km for the supertidal band. The wavenumber ranges are given by dashed black lines in Figure 9. The wavenumber ranges used to compute spectral slopes

in the supertidal band are chosen to be different than those of the other two frequency bands because the large jump in energy seen in the supertidal frequency band generally falls within the mesoscale band, making calculation of slopes over that region impractical. Figure 10a, displaying spectral slopes calculated from the subtidal band, shows that the slopes in five of the seven regions fall approximately within the internal quasi-geostrophy (k^{-5}) and surface quasi-geostophy ($k^{-11/3}$) theoretical slopes [*Stammer*, 1997; *Le Traon et al.*, 2008; *Sasaki and Klein*, 2012], indicated by black horizontal lines labeled QG and SQG, respectively. The slopes calculated from the Kuroshio region (labeled "KU" on the x-axis) are closest to the theoretical interior QG slopes, yet shallower, consistent with previous studies [*Le Traon et al.*, 2008; *Sasaki and Klein*, 2012; *Richman et al.*, 2012]. The North Pacific region (labeled "NP" on the x-axis) shows flatter slopes than the other six regions, and shallower than the SQG prediction, similar to results in *Richman et al.* [2012]. In the tidal band (Figure 10b), the slopes in all regions tend to shift upwards towards the k^{-2} [*Garrett and Munk*, 1972] internal gravity wave line (indicated by a black horizontal line labeled "IGW"). While some of the simulations in the North Atlantic (labelend "NA") have steeper slopes, all other tidal slopes in Figure 10b are shallower than k^{-3}. It should be noted that the *Garrett and Munk* [1972] predictions of k^{-2} are meant to be applicable to the supertidal IGW continuum, and are not necessarily expected to hold for internal tides. In the supertidal band (Figure 10c), the slopes measured span the full range shown, from almost k^{-7} in HYCOM12 in the Equatorial Pacific (labeled "EQPAC") to $\sim k^{-1}$ in all regions in MITgcm48. While there is little consistency regarding which simulation measures the steepest or shallowest slopes in Figures 10a and 10b, there is a clear trend in Figure 10c. Over all seven regions, the HYCOM25 slopes are

always shallower than the HYCOM12 slopes, and the MITgcm slopes become progressively shallower as resolution increases from MITgcm12 to MITgcm24 to MITgcm48. The MITgcm25 slopes generally lie closest to the predicted k^{-2} value, while the MITgcm48 slopes are shallower, hovering around k^{-1}. In the Kuroshio and North Atlantic regions, the supertidal slopes measured in HYCOM12 and HYCOM25 are similar, consistent with what is seen in Figure 9c. In the MITgcm simulations, the difference between the slopes measured in MITgcm12 and MITgcm24 are larger than the difference between slopes in MITgcm24 and MITgcm48 in the North Pacific, the Kuroshio, the Equatorial Pacific, and the North Atlantic regions. In most regions, the spectral slope of the supertidal frequency band computed from both models increases similarly between the $\sim 1/12^\circ$ and $\sim 1/24^\circ$ simulations. While neither HYCOM12 nor MITgcm12 consistently has slopes shallower than the other, the spectral slopes measured from MITgcm24 are consistently shallower than those measured in HYCOM25, except in the North Pacific, that appears as an outlier for HYCOM25 in Figure 10c. In general, the slopes measured from the MITgcm simulations tend to be similar across all regions for each horizontal resolution, but the slopes measured from the HYCOM simulations vary greatly by region, particularly in HYCOM12. Both models need to be compared to more data to discover which, if either, is more closely capturing oceanic IGW dynamics. Figures 9 and 10 suggest that, while these two models show some agreement at frequencies lower than ~ 2 cpd, their differences in wave drag, vertical discretization, subgridscale parametrizations, and resolution have a noticeable effect at high-frequencies that are a component of the small-scale phenomena [*Richman et al.*, 2012; *Callies and Ferrari*, 2013; *Rocha et al.*, 2016a] of interest for the upcoming SWOT altimeter mission.

5. Conclusions

Two-dimensional maps of sea surface height (SSH), from which wavenumber spectral densities can be computed, will soon become available on a global scale via swath satellite altimetry technology, such as the Surface Water and Ocean Topography (SWOT) mission. As in current altimeter technology, swath altimetry will alias high-frequency motions. Here, we use two global general circulation ocean models, varying in horizontal resolution and forced by both atmospheric fields and tides, to study the frequency-horizontal wavenumber spectral density of SSH variance, with specific focus on the contributions from high-frequency motions, such as internal tides and the internal gravity wave (IGW) continuum. Comparison of modeled dynamic height variance in tidal and supertidal frequencies with observed dynamic height variance indicates that both models are well matched to available data at diurnal and semidiurnal frequencies, while HYCOM25 has a low bias in the supertidal band, dominated by the IGW continuum. In this band, the MITgcm lies closer to the observations. This low bias in HYCOM may be due to the lower horizontal and vertical resolution of the HYCOM simulation, to the differences in vertical discretization and/or subgridscale closures, or to the effects of wave drag parametrization in HYCOM.

The frequency-horizontal wavenumber spectral densities of SSH variance, computed over seven regions from five simulations of the two models, at horizontal resolutions ranging from $1/12^\circ$ to $1/48^\circ$, display high variance along the linear dispersion curves of low vertical mode IGWs. This demonstrates that global ocean models such as HYCOM and MITgcm are beginning to resolve SSH signatures of the IGW continuum. We have also shown that increasing the model horizontal resolution increases the modeled IGW continuum SSH

variance. The contributions to SSH wavenumber spectral density from three frequency bands (subtidal, tidal, and supertidal), reiterate the fact that high-frequencies contribute to, and sometimes dominate, the SSH variance at small scales of interest for the SWOT mission. The transition length scale where the supertidal band dominates the SSH variance wavenumber spectral density over the subtidal band is dependent on latitude (where low latitudes tend towards larger transition length scales) and eddy activity (where regions of high eddy activity tend towards smaller transition length scales). This is consistent with the transition length scales for kinetic energy derived from Acoustic Doppler Current Profiler observations, discussed in *Qiu et al.* [2017]. Understanding this transition could be of vital importance to the SWOT mission, that aims to study wavelengths down to 15 km. However, the differences in the HYCOM and MITgcm simulations, such as the presence of a topographic internal wave drag parametrization, differences in horizontal and vertical resolution, differences in vertical discretization schemes, and differences in subgridscale closures all impact the variance measured in the supertidal frequency band at scales ~ 70 km and smaller. More model-observation comparisons, especially at supertidal frequencies, are needed to better understand the output of models that have only recently been shown to partially resolve the IGW continuum. Tidal and supertidal motions, aliased by satellite altimetry, will need to be properly understood and mapped if we are to gain meaningful insight regarding the dynamics of both high- and low-frequency motions at small scales from this upcoming mission.

6. Acknowledgements

We thank the technical teams, captains, and crews of the various ships that deployed and recovered the McLane profilers. ACS acknowledges funding provided by the National

Aeronautics and Space Administration (NASA) Earth and Space Science Fellowship grant NNX16AO23H. BKA, ACS, and JKA acknowledge funding by the University of Michigan Associate Professor Support Fund, supported by the Margaret and Herman Sokol Faculty Awards. ACS and BKA were also funded by the Office of Naval Research (ONR) grants N00014-15-1-2288 and N00014-11-1-0487. JKA and BKA acknowledge funding provided by National Science Foundation (NSF) grant number OCE-0968783. BKA and AKO acknowledge funding provided by NSF grant OCE-1351837. JTF acknowledges funding provided by the NASA grants NNX13AE32G, NNX16AH76G, and NNX13AE46. JGR, JFS, AJW, and LZ are supported by the project "Eddy resolving global ocean prediction including tides" sponsored by the Office of Naval Research. ACS, BKA, JGR, and JFS also acknowledge funding provided by the National Aeronautics and Space Administration grants NNX13AD95Q and NNX16AH79G. We acknowledge ONR and NSF for the support that enabled deployment of the McLane profilers. This NRL contribution NRL/JA/7320–17-3413 has been approved for public release.

While sea surace height fields from HYCOM and MITgcm are too large to host publicly, the sea surface height fields are stored on University of Michigan computers, and will be made freely available to members of the scientific community upon request. Profile data from the McLane profilers and corresponding profiles from HYCOM and MITgcm can be downloaded from `https://github.com/annasavage/McLane_profiler_data`.

References

Alford, M. H., J. A. MacKinnon, Z. Zhao, R. Pinkel, J. Klymak, and T. Peacock (2007), Internal waves across the Pacific, *Geophys. Res. Lett.*, *34*(L24601), doi:

doi:10.1029/2007GL031566.

Alford, M. H., J. A. MacKinnon, J. D. Nash, H. L. Simmons, A. Pickering, J. M. Klymak, R. Pinkel, O. Sun, L. Rainville, R. Musgrave, T. Beitzel, K.-H. Fu, and C.-W. Lu (2011), Energy flux and dissipation in Luzon Strait: Two tales of two ridges, *J. Phys. Oceanogr.*, *41*(11), 2211–2222.

Ansong, J. K., B. K. Arbic, M. C. Buijsman, J. G. Richman, J. F. Shriver, and A. J. Wallcraft (2015), Indirect evidence for substantial damping of low-mode internal tides in the open ocean, *Journal of Geophysical Research Oceans*, *120*, 7997–8019, doi: 10.1002/2015JC010998.

Ansong, J. K., B. K. Arbic, M. C. Buijsman, M. H. Alford, Z. Zhao, L. S. Harper, P. G. Timko, J. G. Richman, E. J. Metzger, J. F. Shriver, and A. J. Wallcraft (2017), Semidiurnal internal tide energy fluxes and their variability in a global ocean model and moored observations, *Journal of Geophysical Research–Oceans*, doi:10.1002/2016JC012184.

Arbic, B. K., A. J. Wallcraft, and E. J. Metzger (2010), Concurrent simulation of the eddying general circulation and tides in a global ocean model, *Ocean Modelling*, *32*, 175–187, doi:10.1016/j.ocemod.2010.01.007.

Arbic, B. K., J. G. Richman, J. F. Shriver, P. G. Timko, E. J. Metzger, and A. J. Wallcraft (2012), Global modeling of internal tides within an eddying ocean general circulation model, *Oceanography*, *25*, 20–29, doi:10.5670/oceanog.2012.38.

Baker-Yeboah, S., D. R. Watts, and D. A. Byrne (2009), Measurements of sea surface height variability in the eastern Atlantic from pressure sensor-equipped inverted echo sounders: baroclinic and barotropic components, *Journal of Atmospheric and Oceanic Technology*, *26*, 2593–2609, doi:10.1175/2009JTECHO659.1.

Buijsman, M. C., B. K. Arbic, J. A. M. Green, R. W. Helber, J. G. Richman, J. F. Shriver, P. G. Timko, and A. J. Wallcraft (2015), Optimizing internal wave drag in a forward barotropic model with semidiurnal tides, *Ocean Modelling*, *85*, 42–55.

Buijsman, M. C., J. K. Ansong, B. K. Arbic, J. G. Richman, J. F. Shriver, P. G. Timko, A. J. Wallcraft, C. B. Whalen, and Z. Zhao (2016), Impact of parameterized internal wave drag on the semidiurnal energy balance in a global ocean circulation model, *Journal of Physical Oceanography*, *46*, doi:10.1175/JPO-D-15-0074.1.

Callies, J., and R. Ferrari (2013), Interpreting energy and tracer spectra of upper-ocean turbulence in the submesoscale range (1-200 km), *Journal of Physical Oceanography*, *43*, doi:10.1175/JPO-D-13-063.1.

Cartwright, D. E. (1999), *Tides: A Scientific History*, 192 pp., Cambridge Univ. Press, Cambridge, U. K.

Chassignet, E. P., H. E. Hurlburt, E. J. Metzger, O. M. Smedstad, J. A. Cummings, G. R. Halliwell, R. Bleck, R. Baraille, A. J. Wallcraft, C. Lozano, H. L. Tolman, A. Srinivasan, S. Hankin, P. Cornillon, R. Weisberg, A. Barth, R. He, F. Werner, and J. Wilkin (2009), Global ocean prediction with the HYbrid Coordinate Ocean Model (HYCOM), *Oceanography*, *22*, 64–76.

D'Asaro, E. A. (1984), Wind forced internal waves in the north pacific and sargasso sea, *Journal of Physical Oceanography*, *14*, 781–794.

Dee, D. P., S. M. Uppala, A. J. Simmons, P. Berrisford, P. Poli, S. Kobayashi, U. Andrae, M. A. Balmaseda, G. Balsamo, P. Bechtold, A. C. M. Beljaars, L. van de Berg, J. Bidlot, N. Bormann, C. Delsol, R. Dragani, M. Fuentes, A. J. Geer, L. Haimberger, S. B. Healy, H. Hersbach, E. V. Hólm, L. Isaksen, P. Kållberg, M. Köhler, M. Matricardi,

A. P. McNally, B. M. Monge-Sanz, J.-J. Morcrette, B.-K. Park, C. Peubey, P. de Rosnay, C. Tavolato, J.-N. Thépaut, and F. Vitart (2011), The ERA-interim reanalysis: Configuration and performance of the data assimilation system, *Quarterly Journal of The Royal Meteorological Society*, *137*, 553–597, doi:10.1002/qj.828.

Doherty, K. W., D. E. Frye, S. P. Liberatore, and J. M. Toole (1999), A moored profiling instrument, *Journal of atmospheric and ocean technology*, *16*, 1816–1829, doi: http://dx.doi.org/10.1175/1520-0426(1999)016¡1816:AMPI¿2.0.CO;2.

Egbert, G. D., A. F. Bennett, and M. G. G. Foreman (1994), TOPEX/POSEIDON tides estimated using a global inverse model, *Journal of Geophysical Research*, *99*, 24,821–24,852.

Erofeeva, S. Y., G. D. Egbert, and P. M. Kosro (2003), Tidal currents on the central Oregon coast: Models, data, and assimilation, *Journal of Geophysical Research*, *108*, doi:10.1029/2002JC001615.

Ferrari, R., and C. Wunsch (2009), Ocean circulation kinetic energy: Resevoirs, sources, and sinks, *Annual Review of Fluid Mechanics*, *41*, 253–282, doi: 10.1146/annurev.fluid.40.111406.102139.

Fu, L. L., D. Alsdorf, R. Morrow, E. Rodriguez, and N. Mognard (Eds.) (2012), *SWOT: The Surface Water and Ocean Topography Mission: Wide-Swatch Altimetric Measurement of Water Elevation on Earth, JPL-Publication*, 228 pp., Jet Propul. Lab., Pasadena, Calif.

Garrett, C., and W. Munk (1972), Space-time scales of internal waves, *Journal of Geophysical Research*, *2*, 225–264.

Glazman, R. E., and B. Cheng (1999), Altimeter observations of baroclinic oceanic inertia-gravity wave turbulence, *Proceedings of the Royal Society A*, *455*, 90–123, doi: 10.1098/rspa.1999.0304.

Harris, F. J. (1976), Windows, harmonic analysis, and the discrete Fourier transform, Undersea Surveillance Department, Naval Undersea Center, San Diego, CA.

Hendershott, M. C. (1972), The effects of solid earth deformation on global ocean tides, *Geophys. J. R. Astron. Soc.*, *29*, 389–402, doi:10.1111/j.1365-246X.1972.tb06167.x.

Hogan, T. F., M. Liu, J. A. Ridout, M. S. Peng, T. R. Whitcomb, B. C. Ruston, C. A. Reynolds, S. D. Eckermann, J. R. Moskaitis, N. L. Baker, J. P. McCormack, K. C. Viner, J. G. McLay, M. K. Flatau, L. Xu, C. Chen, and S. W. Chang (2014), The Navy Global Environemental Model, *Oceanography*, *27*, 116–125, doi:10.5670/oceanog.2014.73.

Jakobsson, M., R. Macnab, L. Mayer, R. Anderson, M. Edwards, J. Hatzky, H. W. Schenke, and P. Johnson (2008), An improved bathymetric portrayal of the Arctic Ocean: implications for ocean modeling and geological, geophysical and oceanographic analyses, *Geophysical Research Letters*, *35*, doi:10.1029/2008GL033520.

Jan, S., R. Lien, and C. Ting (2008), Numerical study of baroclinic tides in Luzon Strait, *Journal of Oceanography*, *64*, 789–802, doi:10.1007/s10872-008-0066-5.

Jayne, S. R., and L. C. St. Laurent (2001), Parameterizing tidal dissipation over rough topography, *Geophysical Research Letters*, *28*, 811–814.

Knauss, J. A. (1997), *Introduction to Physical Oceanography*, 2nd ed., Waveland Press, Inc., Long Grove, IL.

Large, W. G., and S. G. Yeager (2004), Diurnal and decadal global forcing for ocean and sea-ice models: The data sets and climatologies, NCAR Tech. Note, Boulder, CO, 105

pp., doi:10.5065/D6KK98Q6, tN–460+ST (May).

Le Traon, P. Y., P. Klein, B. L. Hua, and G. Dibarboure (2008), Do altimeter wavenumber spectra agree with the interior or surface quasi-geostrophic theory?, *Journal of Physical Oceanography*, *38*, 1137–1142, doi:10.1175/2007JPO3806.1.

Losch, M., D. Menemenlis, J.-M. Campin, P. Heimbach, and C. N. Hill (2010), On the formulation of sea-ice models. Part 1: effects of different solver implementations and parameterizations, *Ocean Modelling*, *33*, 129–144, doi:10.1016/j.ocemod.2009.12.008.

Lumley, J. L. (1970), *Stochastic Tools in Turbulence*, 100 pp., Dover Publications, Inc., Mineola, NY.

MacKinnon, J. A., M. H. Alford, R. Pinkel, J. Klymak, and Z. Zhao (2013a), The latitudinal dependence of shear and mixing in the Pacific transiting the critical latitude for PSI, *J. Phys. Oceanogr.*, *43*(1), 3–16.

MacKinnon, J. A., M. H. Alford, O. Sun, R. Pinkel, Z. Zhao, and J. Klymak (2013b), Parametric Subharmonic Instability of the internal tide at 29N, *J. Phys. Oceanogr.*, *43*(1), 17–28.

Marshall, J., A. Adcroft, C. Hill, L. Perelman, and C. Heisey (1997), A finite-volume, incompressible navier stokes model for studies of the ocean on parallel computers, *Journal of Geophysical Research*, *102*, 5753–5766, doi:10.1029/96JC02775.

Martini, K. I., M. H. Alford, S. Kelly, and J. D. Nash (2011), Observations of internal tides on the Oregon Continental Slope, *J. Phys. Oceanogr.*, *41*(9), 1772–1794.

Martini, K. I., M. H. Alford, E. Kunze, S. M. Kelly, and J. D. Nash (2013), Internal bores and breaking internal tides on the Oregon continental slope, *J. Phys. Oceanogr.*, *43*(1), 120–141.

Menemenlis, D., J.-M. Campin, P. Heimbach, C. N. Hill, T. Lee, A. T. Nguyen, M. P. Schodlok, and H. Zhang (2008), ECCO2: High resolution global ocean and sea ice data synthesis, Mercator Ocean Quarterly Newsletter, 13–21 pp.

Müller, M., B. K. Arbic, J. G. Richman, J. F. Shriver, E. L. K. R. B. Scott, A. J. Wallcraft, and L. Zamudio (2015), Toward and internal gravity wave spectrum in global ocean models, *Geophysical Research Letters*, *42*, 3474–3481, doi:10.1002/2015GL063365.

Munk, W. (1981), Internal waves and small-scale processes, in *Evolution of Physical Oceanography: Scientific Surveys in Honor of Henry Stommel*, chap. 9, pp. 264–291, The MIT Press, Cambridge and London.

Munk, W., and C. Wunsch (1998), Abysall recipes II: energetics of tidal and wind mixing, *Deep Sea Research Part 1 Oceanographic Research Papers*, *45*, 1977–2010.

Nash, J. D., M. H. Alford, E. Kunze, K. I. Martini, and S. Kelly (2007), Hotspots of deep ocean mixing on the Oregon continental slope, *Geophys. Res. Lett.*, *34*(L01605), doi:10.1029/2006GL028,170.

Ngodock, H. E., I. Souopgui, A. J. Wallcraft, J. G. Richman, J. F. Shriver, and B. K. Arbic (2016), On improving the accuracy of the M_2 barotropic tides embedded in a high-resolution global ocean circulation model, *Ocean Modelling*, *97*, 16–26, doi: 10.1016/j.ocemod.2015.10.011.

Ponte, R. M., A. H. Chaudhuri, and S. V. Vinogradov (2015), Long-period tides in an atmospherically driven, stratified ocean, *Journal of Physical Oceanography*, *45*, 1917–1928, doi:10.1175/JPO-D-15-0006.1.

Qiu, B., T.Nakano, S. Chen, and P. Klein (2017), Submesoscale transition from geostrophic flows to internal waves in the northwestern Pacific upper ocean, *Nature*

Communications, doi:10.1038/ncomms14055.

Ray, R. D. (1999), A global ocean tide model from TOPEX/POSEIDON altimetry: GOT99.2., National Aeronautics and Space Administration Technical Memorandum, 58pp pp., nASA/TM-1999-209478.

Ray, R. D., and D. A. Byrne (2010), Bottom pressure tides along a line in the southern Atlantic Ocean and comparisons with satellite altimetry, *Ocean Dynamics*, *60*, 1167–1176, doi:10.1007/s10236-010-0316-0.

Ray, R. D., and G. T. Mitchum (1997), Surface manifestation of internal tides in the deep ocean: observations from altimetry and island gauges, *Prog. Oceanog.*, *40*, 135–162, doi:10.1016/S0079-6611(97)00025-6.

Ray, R. D., and E. D. Zaron (2016), M_2 internal tides and their observed wavenumber spectra from satellite altimetry, *Journal of Physical Oceanography*, *46*, 3–22, doi:10.1175/JPO-D-15-0065.1.

Richman, J. G., B. K. Arbic, J. F. Shriver, E. J. Metzger, and A. J. Wallcraft (2012), Inferring dynamics from the wavenumber spectra of an eddying global ocean model with embedded tides, *Journal of Geophysical Research*, *117*, doi:10.1029/2012JC008364.

Rocha, C. B., T. K. Chereskin, S. T. Gille, and D. Menemenlis (2016a), Mesoscale to submesoscale wavenumber spectra in Drake Passage, *Journal of Physical Oceanography*, *46*, doi:10.1175/JPO-D-15-0087.1.

Rocha, C. B., S. T. Gille, T. K. Chereskin, and D. Menemenlis (2016b), Seasonality of submesoscale dynamics in the Kuroshio Extension, *Geophysical Research Letters*, doi:10.1002/2016GL071349.

Sasaki, H., and P. Klein (2012), Ssh wavenumber spectra in the north pacific from a high-resolution realistic simulation, *Journal of Physical Oceanography*, *42*, 1233–1241, doi:10.1175/JPO-D-11-0180.1.

Savage, A. C., B. K. Arbic, J. G. Richman, J. F. Shriver, M. H. Alford, M. C. Buijsman, J. T. Farrar, H. Sharma, G. Voet, A. J. Wallcraft, and L. Zamudio (2017), Frequency content of sea surface height variability from internal gravity waves to mesoscale eddies, *Journal of Geophysical Research–Oceans*, doi:10.1002/2016JC012331.

Shriver, J. F., B. K. Arbic, J. G. Richman, R. D. Ray, E. J. Metzger, A. J. Wallcraft, and P. G. Timko (2012), An evaluation of the barotropic and internal tides in a high resolution global ocean circulation model, *Journal of Geophysical Research*, *17*, doi: 10.1029/2012JC008170.

Smith, W. H. F., and D. T. Sandwell (1997), Global sea floor topography from satellite altimetry and ship depth soundings, *Science*, *277*, 1956–1962, doi: 10.1126/science.277.5334.1956.

Soufflet, Y., P. Marchesiello, F. Lemarié, J. Jouanno, X. Capet, L. Debreu, and R. Benshila (2016), On effective resolution in ocean models, *Ocean MOdelling*, *98*, 36–50, doi:http://dx.doi.org/10.1016/j.ocemod.2015.004.

Stammer, D. (1997), Global characteristics of ocean variability estimated from regional TOPEX/poseidon altimeter measurements, *Journal of Physical Oceanography*, *27*, 1743–1769, doi:10.1175/1520-0485(1997)027¡1743:GCOOVE¿2.0.CO;2.

Stammer, D., R. D. Ray, O. B. Andersen, B. K. Arbic, W. Bosch, L. Carrèrre, Y. Cheng, D. S. Chinn, B. D. Dushaw, G. D. Egbert, S. Y. Erofeeva, H. S. Fok, J. A. M. Green, S. Griffiths, M. A. King, V. Lapin, F. G. Lemoine, S. B. Luthcke, F. Lyard, J. Morison,

M. Müller, L. Padman, J. G. Richman, J. F. Shriver, C. K. Shum, E. Taguchi, and Y. Yi (2014), Accuracy assessment of global barotropic ocean tide models, *Reviews of Geophysics*, *52*, 243–282, doi:10.1002/2014RG000450.

Timko, P. G., B. K. Arbic, J. G. Richman, R. B. Scott, E. J. Metzger, and A. J. Wallcraft (2012), Skill test of three-dimensional tidal currents in global ocean model: A look at the North Atlantic, *Journal of Geophysical Research*, *117*, doi:10.1029/2011JC007617.

Timko, P. G., B. K. Arbic, J. G. Richman, R. B. Scott, E. J. Metzger, and A. J. Wallcraft (2013), Skill testing a three-dimensional global tide model to historical current meter records, *Journal of Geophysical Research*, *118*, 6914–6933, doi:10.1002/2013JC009071.

Whalen, C. B., L. D. Talley, and J. A. MacKinnon (2012), Spatial and temporal variability of global ocean mixing inferred from Argo profiles, *Geophysical Research Letters*, *39*, doi:10.1029/2012GL053196.

Xu, Y., and L.-L. Fu (2012), The effects of altimeter instrument noise on the estimation of the wavenumber spectrum of sea surface height, *Journal of Physical Oceanography*, *42*, 2229–2233, doi:10.1175/JPO-D-12-0106.1.

Zantopp, R. J., and K. D. Leaman (1984), The feasibility of dynamic height determination from moored temperature sensors, *Journal of Physical Oceanography*, *14*, 1399–1406.

Zhao, Z., M. H. Alford, J. A. MacKinnon, and R. Pinkel (2010), Long-range propagation of the semidiurnal internal tide from the Hawaiian Ridge, *J. Phys. Oceanogr.*, *40*(4), 713–736.

Zhao, Z., M. H. Alford, J. B. Girton, L. Rainville, and H. L. Simmons (2016), Global observations of open-ocean mode-1 M_2 internal tides, *Journal of Physical Oceanography*, *46*, 1657–1684, doi:10.1175/JPO-D-15-0105.1.

Profiler	Mooring name	Longitude	Latitude	Min. Pressure	Max. Pressure	Start Date	Record Length
a	IWAP MP1	$194.8°E$	$25.5°N$	97	1403	Apr 25, 2006	36
b	IWAP MP3	$196.5°E$	$28.9°N$	97	1418	May 10, 2006	34
c	IWAP MP4	$197.1°E$	$30.1°N$	97	1430	Apr 25, 2006	22
d	IWAP MP6	$200.8°E$	$37.1°N$	97	1410	Apr 25, 2006	22
e	IWISE HO4	$121.0°E$	$19.3°N$	373	1223	June 17, 2011	51
f	SCS MP1	$117.9°E$	$20.9°E$	111	1303	May 6, 2007	31
g	ORE MP1	$233.7°E$	$43.2°N$	138	2121	Sept 15, 2005	40
h	ORE MP4	$234.9°E$	$43.9°N$	73	1332	Sept 14, 2005	40
i	ORE MP5	$235.0°E$	$43.2°N$	236	1063	Sept 13, 2005	40

Table 1. Instrument name, location, minimum and maximum pressures (db), start date, and record length (days) for each of the nine McLane profilers used in this study. Profilers a-d are located in the central North Pacific near Hawai'i, profilers e and f are located in the Luzon Strait, and profilers g-i are located off the Oregon coast of the United States.

Model	Horizontal resolution	Record times	Effective resolution
HYCOM12	1/12.5°	October 1, 2011-September 31, 2012	27 km
HYCOM25	1/25°	January 1, 2014-December 31, 2014	13 km
MITgcm12	1/12°	March 1, 2014-May 29, 2014	28 km
MITgcm24	1/24°	October 31, 2011-January 28, 2012	14 km
MITgcm48	1/48°	October 31, 2011-January 28, 2012	7 km

Table 2. Horizontal resolution, record times, and estimated effective resolution of the five simulations used to compute frequency-horizontal wavenumber spectral densities.

Region	Abbreviation	Longitude range	Latitude range	Average transition length scale
North Pacific	NP	200.0° E–220.0° E	25.0° N–45.0° N	80.0 km
South East Pacific	SEP	260.0° E–279.9° E	18.6° S–37.9° S	58.3 km
Kuroshio	KU	145.0° E–169.9° E	27.0° N–39.7° N	22.7 km
Equatorial Pacific	EQPAC	204.2° E–218.3° E	3.4° S–3.4° N	124.2 km
South Pacific	SP	200.0° E–220.0° E	20.3° S–40.0° S	53.6 km
North Atlantic	NA	297.4° E–321.66° E	22.0° N–41.8° N	37.8 km
Indian Ocean	IND	63.0° E–83.0° E	0°-19.0° S	120.0 km

Table 3. Longitudinal and latitudinal ranges of the seven boxes used for calculation of frequency-horizontal wavenumber spectral densities. The second column lists the abbreviation for each region used in Figures 2 and 10. The final column lists the average transition length scale across all five simulations and is discussed in Section 4.3.

Profiler	a	b	c	d	e	f	g	h	i
Diurnal									
McLane Profiler	0.541	0.144	0.154	0.160	2.039	2.930	0.078	0.302	0.207
HYCOM25	0.415	0.160	0.123	0.033	2.144	2.008	0.025	0.323	0.226
MITgcm48	0.576	0.178	0.119	0.029	3.178	2.048	0.040	0.366	0.305
Semidiurnal									
McLane Profiler	1.869	1.969	0.573	0.654	1.239	2.713	0.333	0.263	0.367
HYCOM25	2.075	1.277	1.049	0.565	1.013	3.577	0.545	0.533	0.324
MITgcm48	2.461	1.047	1.153	0.707	1.194	4.534	0.445	0.644	0.467
Supertidal									
McLane Profiler	0.587	0.433	0.512	0.782	0.486	1.687	0.265	0.471	0.226
HYCOM25	0.335	0.292	0.310	0.493	0.504	2.147	0.139	0.136	0.079
MITgcm48	0.559	0.555	0.446	0.497	0.693	3.142	0.424	0.390	0.252

Table 4. Standard deviation of dynamic height variance (cm) at each profiler location for McLane profiler, HYCOM25, and MITgcm48 in diurnal, semidiurnal, and supertidal frequency bands.

Figure 1. Density anomaly profile time series (kg/m^3) over the pressure intervals sampled by the McLane profiler located at 233.7°E 43.2°N from (a) a McLane profiler, (b) HYCOM25, and (c) MITgcm48. The bottom row displays time series of dynamic height anomaly (cm) computed as in equation (1) for (d) a McLane profiler, (e) HYCOM25, (f) MITgcm48. Data is shown from the first 200 hours of each dataset, and is therefore shown over different time intervals (September for (a) and (d), January for (b) and (e), and October for (c) and (f)).

Figure 2. (a) HYCOM25 bathymetries (m) from seven regions used to compute frequency-horizontal wavenumber spectral densities overlaid on map of regions. Bathymetries from MIT-gcm48 are comparable. Abbreviations for the regions are listed in Table 3. Locations of nine McLane profilers are overlaid on map as red stars. (b) Low frequency SSH variance (cm^2) from HYCOM25 computed as in *Savage et al.* [2017] in seven regions used in study.

Figure 3. Dynamic height variance frequency spectral densities from McLane profilers and nearest neighbor HYCOM25 and MITgcm48 gridpoints. The dashed vertical lines denote K_1 diurnal and M_2 semidiurnal tidal frequencies. The shaded regions are the 95% confidence intervals, that account only for random error in spectral density calculations.

Figure 4. Scatter plots of band-integrated dynamic height variance vs. McLane profilers in 1/25° HYCOM and 1/48° MITgcm in (a) diurnal, (b) semidiurnal, and (c) supertidal frequency bands. Letters on scatter plots correspond to profiler locations listed in Table 1.

Figure 5. Sea surface height variance frequency-horizontal wavenumber spectral density [$cm^2/(cpd\,cpkm)$] computed over seven regions from MITgcm48. Wavenumber axes are set to the maximum wavenumber for each region computed in HYCOM25. White curves show theoretical IGW linear dispersion relations for first (solid), second (dashed), and third (dashed-dotted) vertical modes. Bounding curves for each vertical mode are computed from the maximal and minimal eigenspeeds along the northern and southern boundaries, as in *Müller et al.* [2015].

Figure 6. Sea surface height variance frequency-horizontal wavenumber spectral density of [$cm^2/(cpd\,cpkm)$] computed in North Pacific region in all five simulations. Wavenumber axes are the same in each plot, and are set to the maximum wavenumber for the HYCOM25 calculation. White curves show theoretical IGW linear dispersion relations for first (solid), second (dashed), and third (dashed-dotted) vertical modes. Bounding curves for each vertical mode are computed from the maximal and minimal eigenspeeds along the northern and southern boundaries, as in *Müller et al.* [2015].

Figure 7. Horizontal wavenumber spectral density of SSH variance in all regions in MITgcm48 integrated over subtidal, tidal, and supertidal frequency bands (see text for definition of bands). The 95% confidence intervals span 76% to 137% of shown value for the subtidal band, 85% to 119% for the tidal band, and 94% to 107% for the supertidal band. Right-hand axis shows ratio of supertidal to total SSH variance as a function of isotropic wavenumber.

Figure 8. Horizontal wavenumber spectral density of SSH variance in Kuroshio region integrated over subtidal, tidal, and semidiurnal frequency bands in all five simulations. See text for definition of bands. The 95% confidence intervals span 76% to 137% of shown value for the subtidal band, 85% to 119% for the tidal band, and 94% to 107% for the supertidal band. Right-hand axis shows ratio of supertidal to total SSH variance as a function of isotropic wavenumber.

Figure 9. Horizontal wavenumber spectral density in Kuroshio and North Pacific regions integrated over subtidal, tidal, and semidiurnal frequency bands in all five simulations separated by frequency band. See text for definition of bands. The 95% confidence intervals span 76% to 137% of shown value for the subtidal band, 85% to 119% for the tidal band, and 94% to 107% for the supertidal band. The wavenumbers between the dashed lines were used to compute spectral slopes.

Figure 10. Spectral slopes computed from all five simulations in the (a) subtidal, (b) tidal, and (c) supertidal frequency bands. Slopes were computed over wavenumbers ranging from 1/250-1/70 cpkm in the subtidal and tidal bands, and over wavenumbers ranging from 1/70-1/30 cpkm in the supertidal band. Abbreviations for the regions are listed in Table 3.

Figure 1.

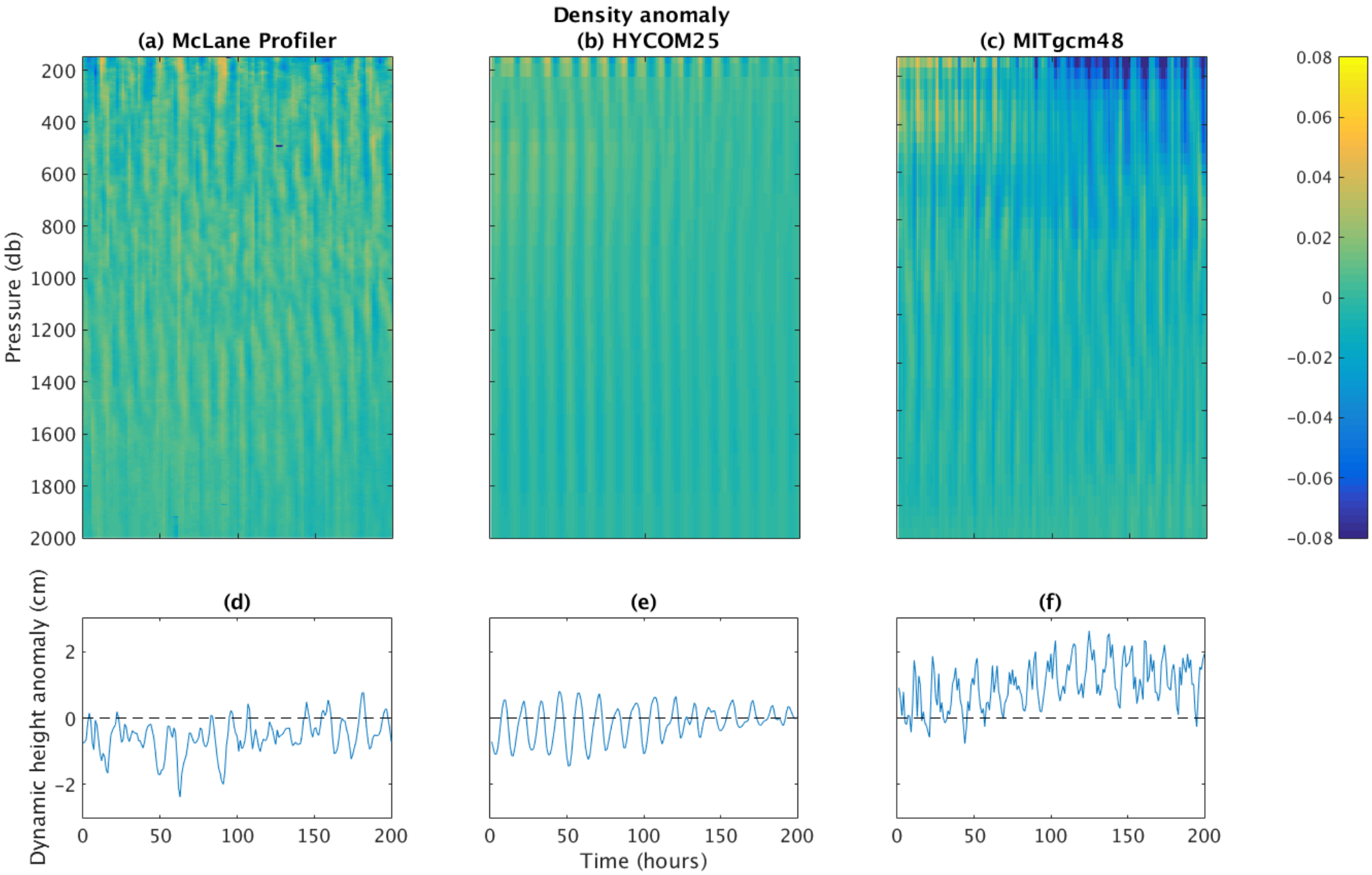

Figure 2.

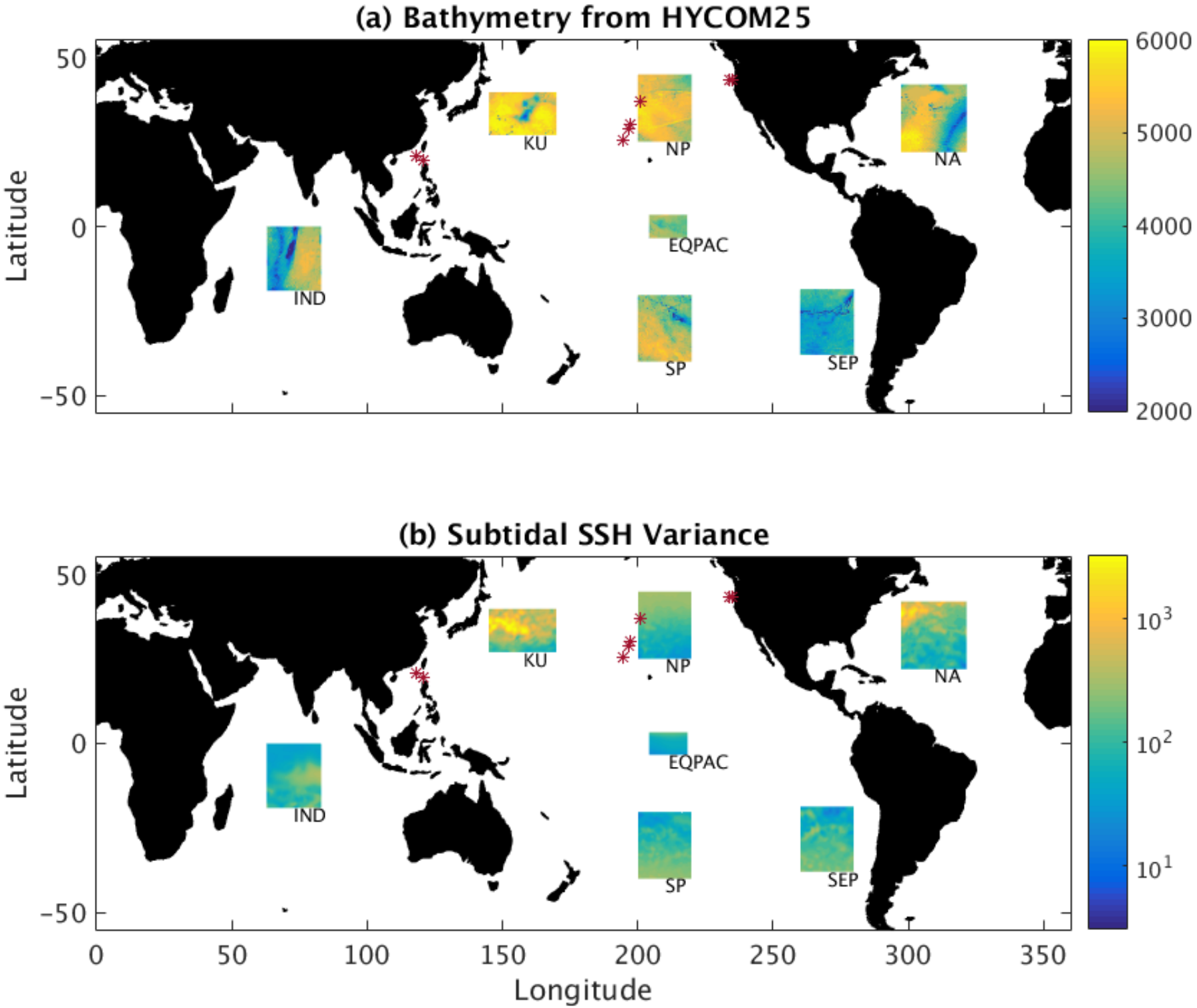

Figure 3.

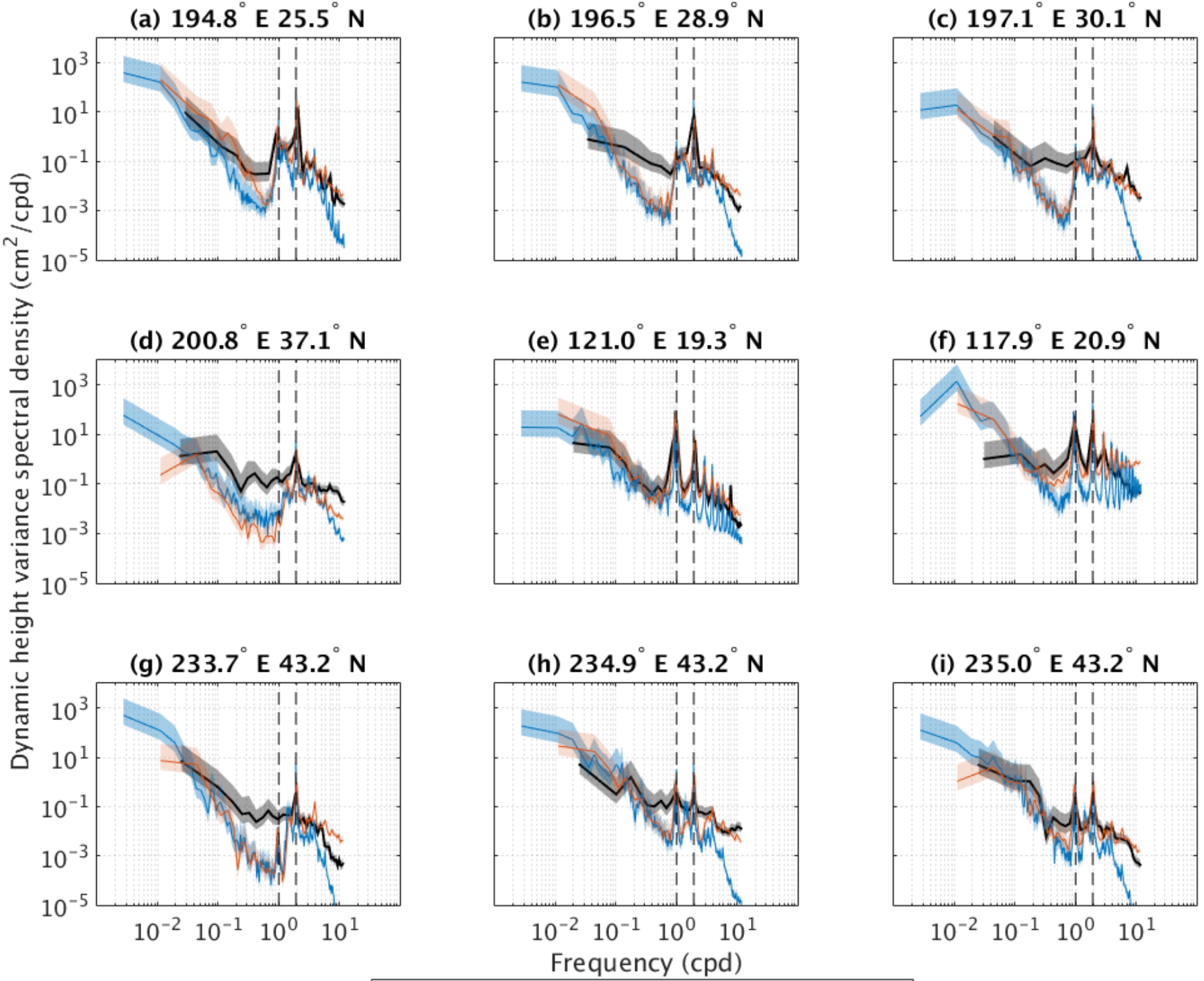

Figure 4.

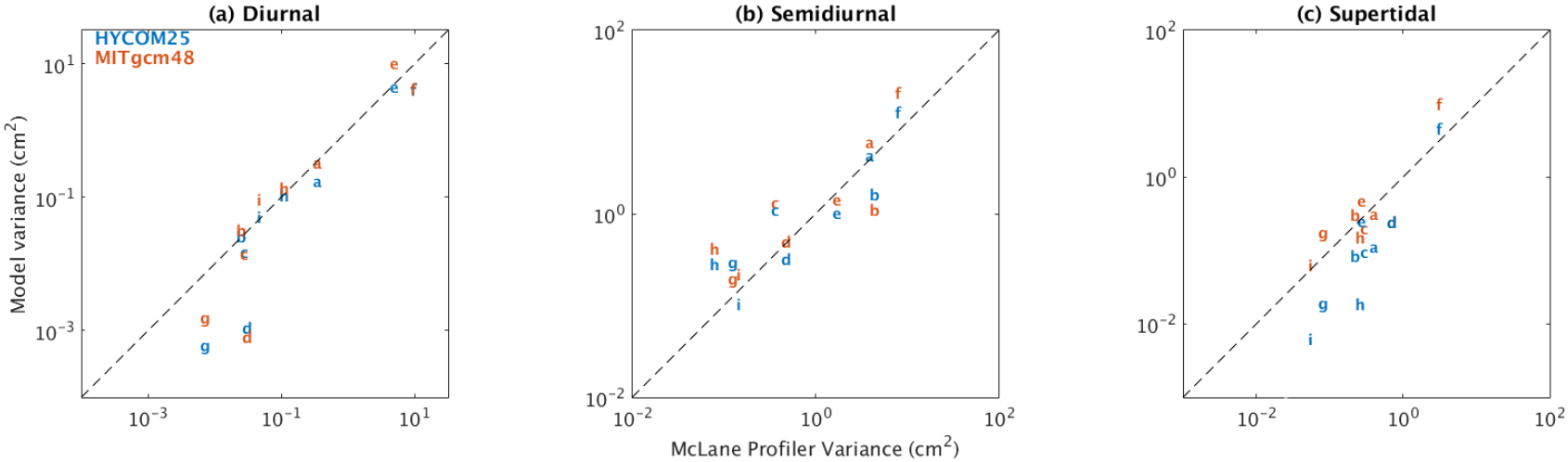
(a) Diurnal
HYCOM25
MITgcm48
Model variance (cm^2)
10^{1}
10^{-1}
10^{-3}
10^{-3}
10^{-1}
10^{1}
(b) Semidiurnal
10^{2}
10^{0}
10^{-2}
10^{-2}
10^{0}
10^{2}
McLane Profiler Variance (cm^2)
(c) Supertidal
10^{2}
10^{0}
10^{-2}
10^{-2}
10^{0}
10^{2}

Figure 5.

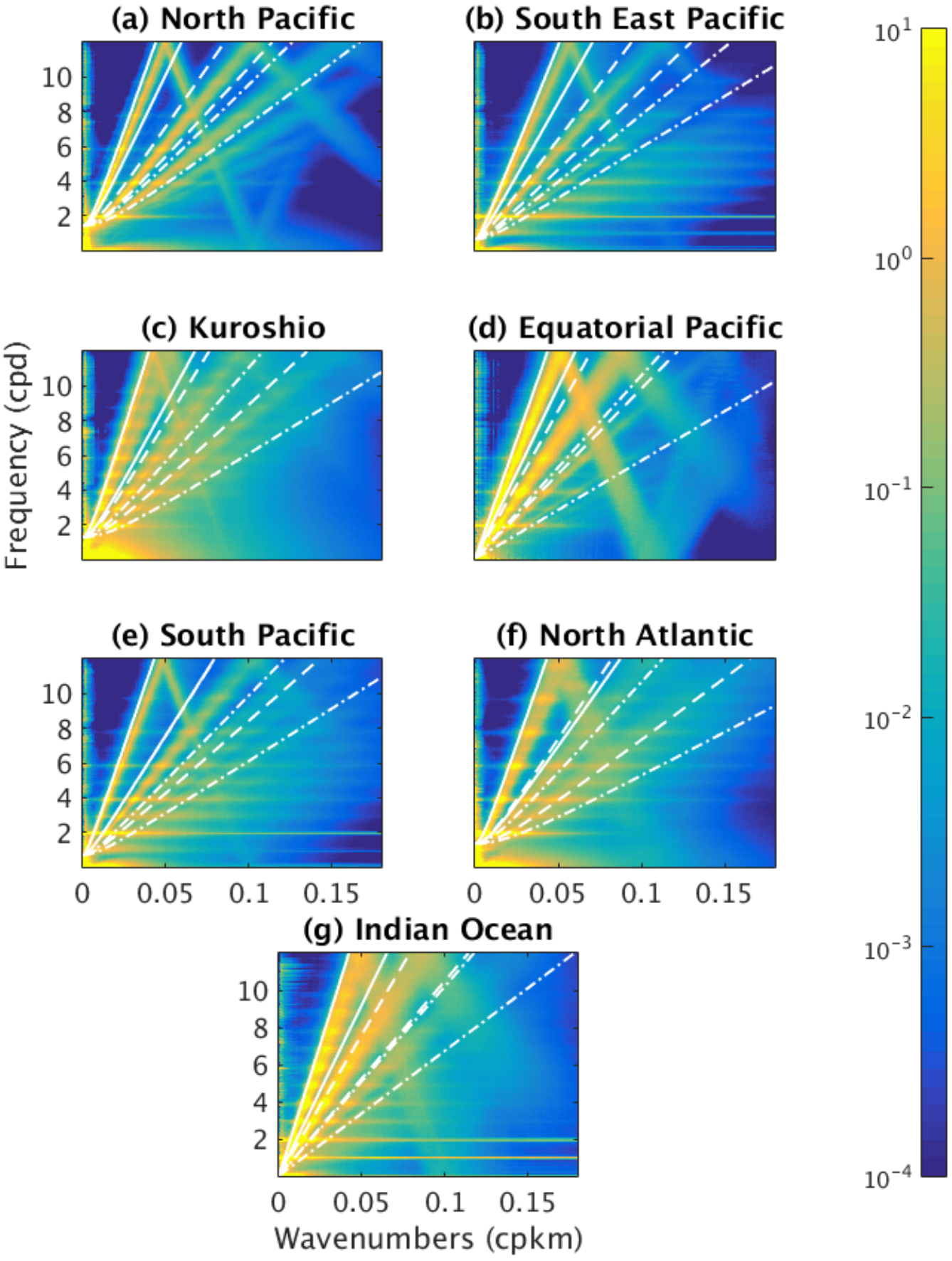

Figure 6.

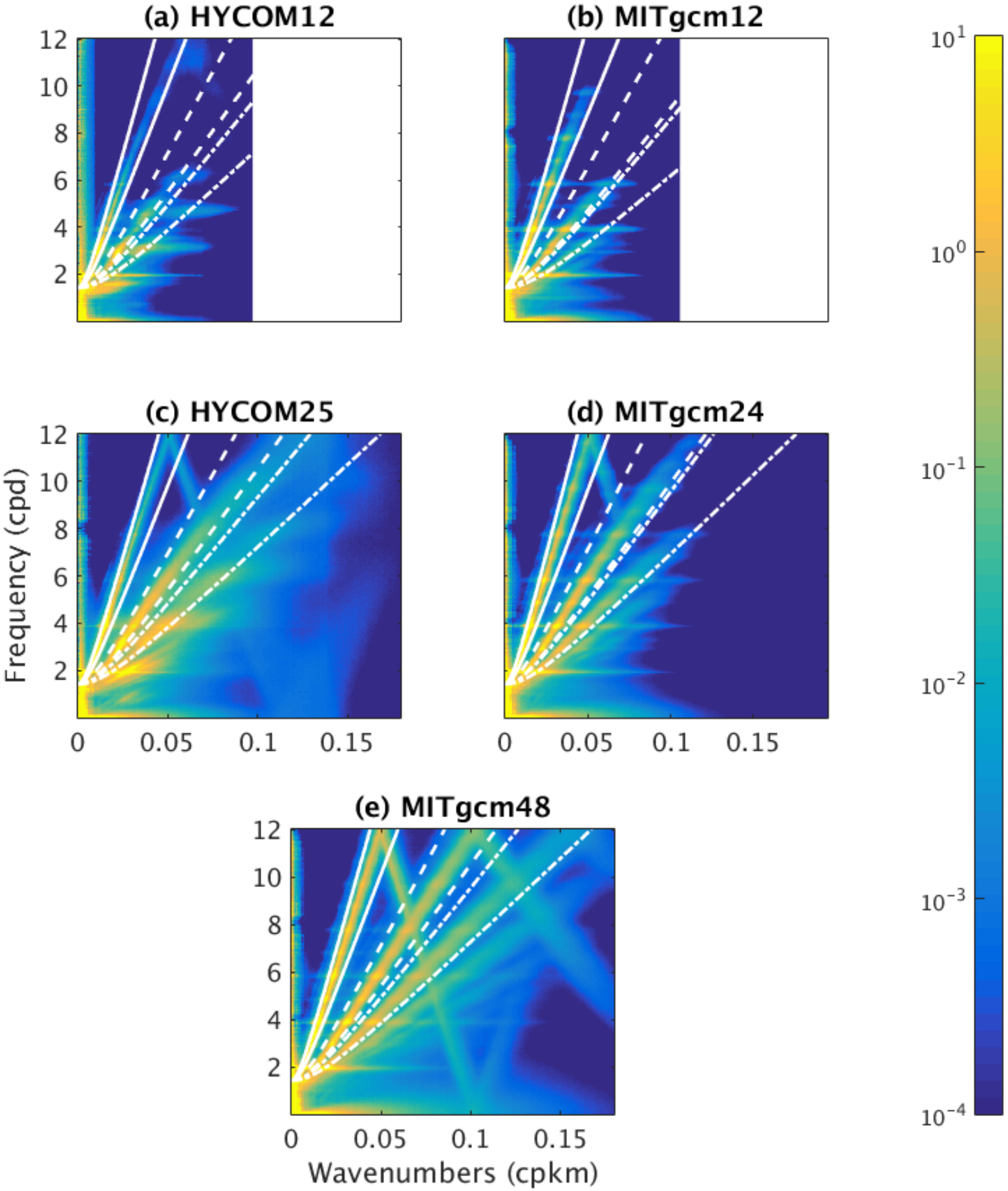

Figure 7.

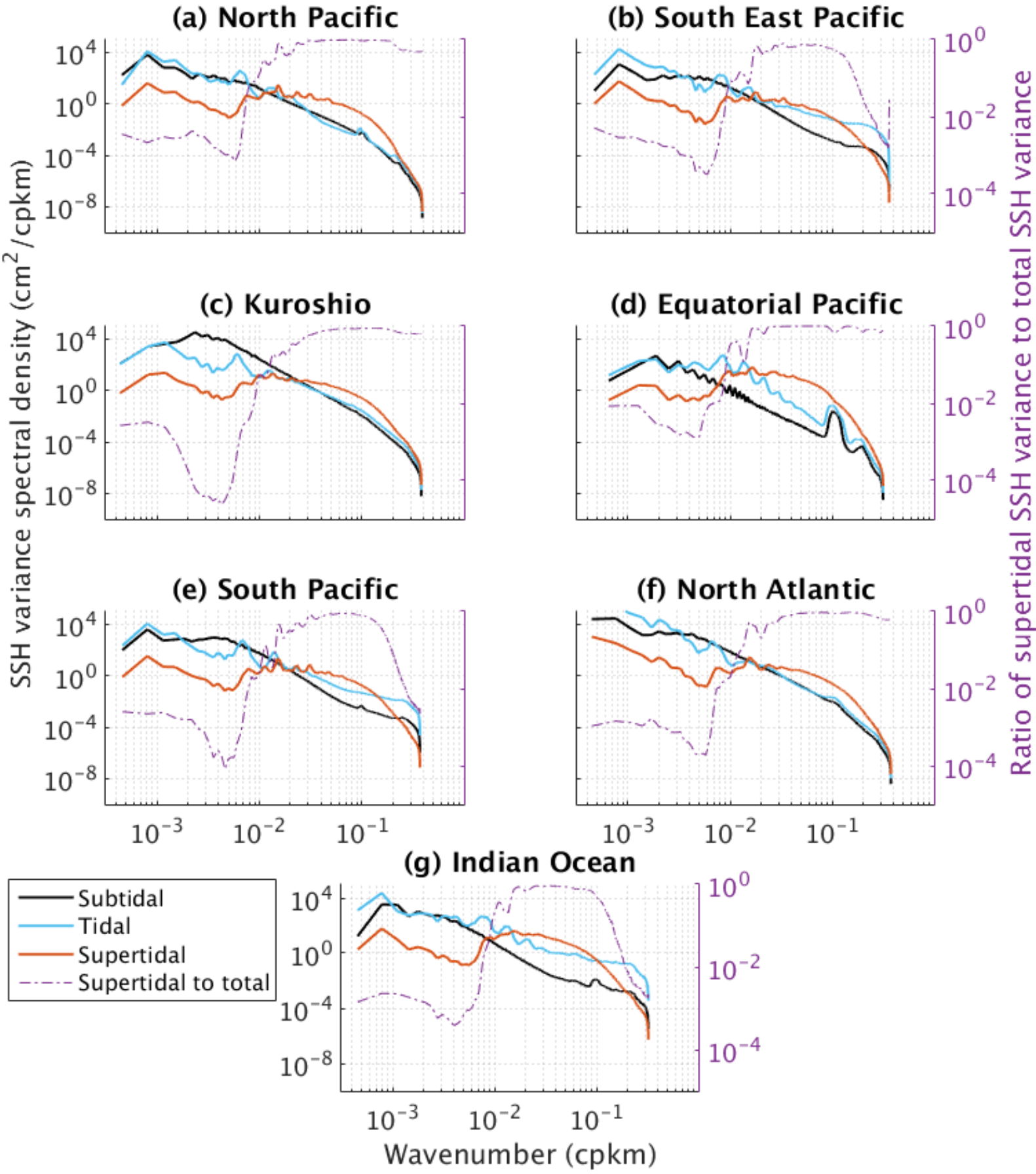

Figure 8.

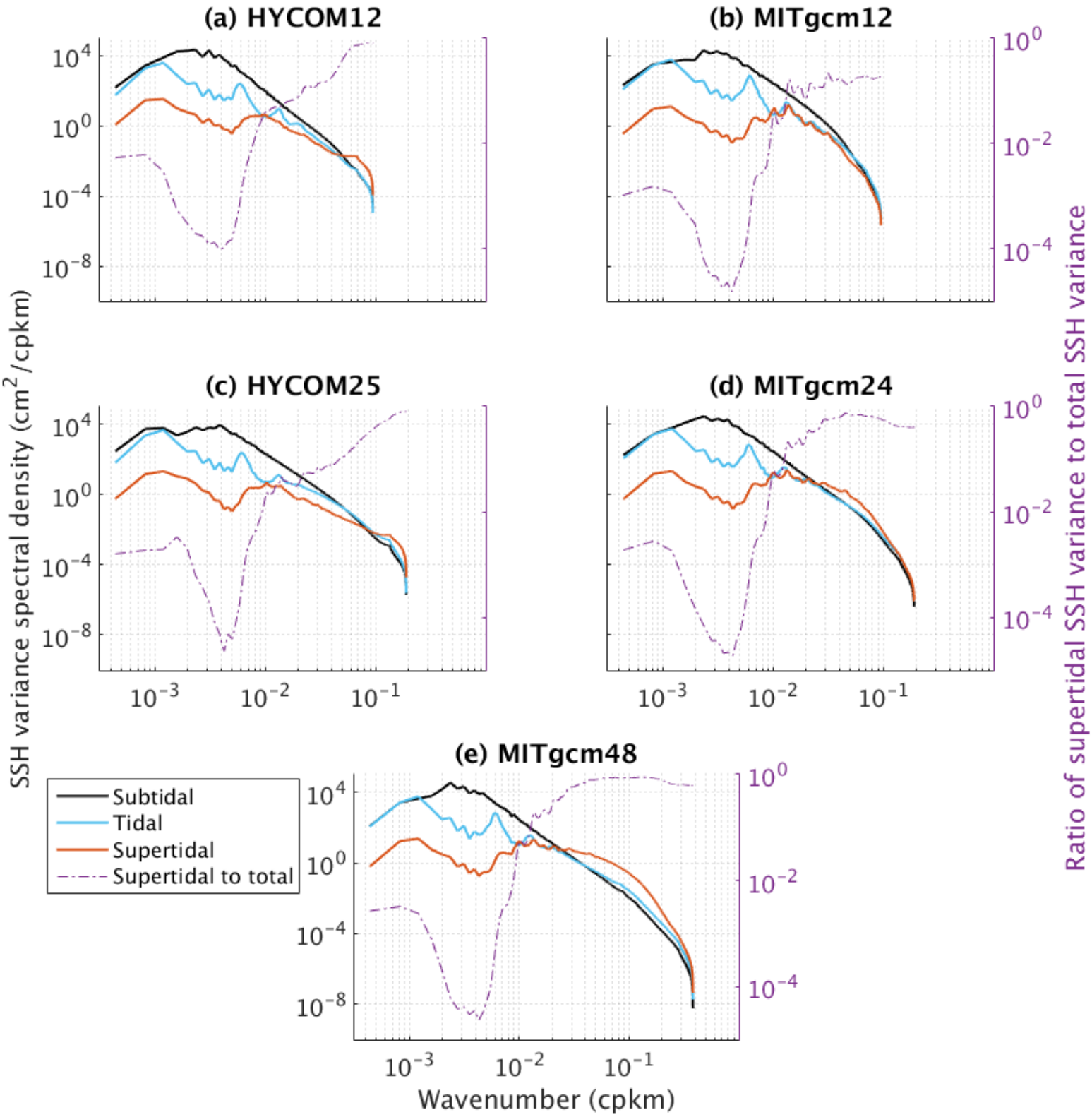

Figure 9.

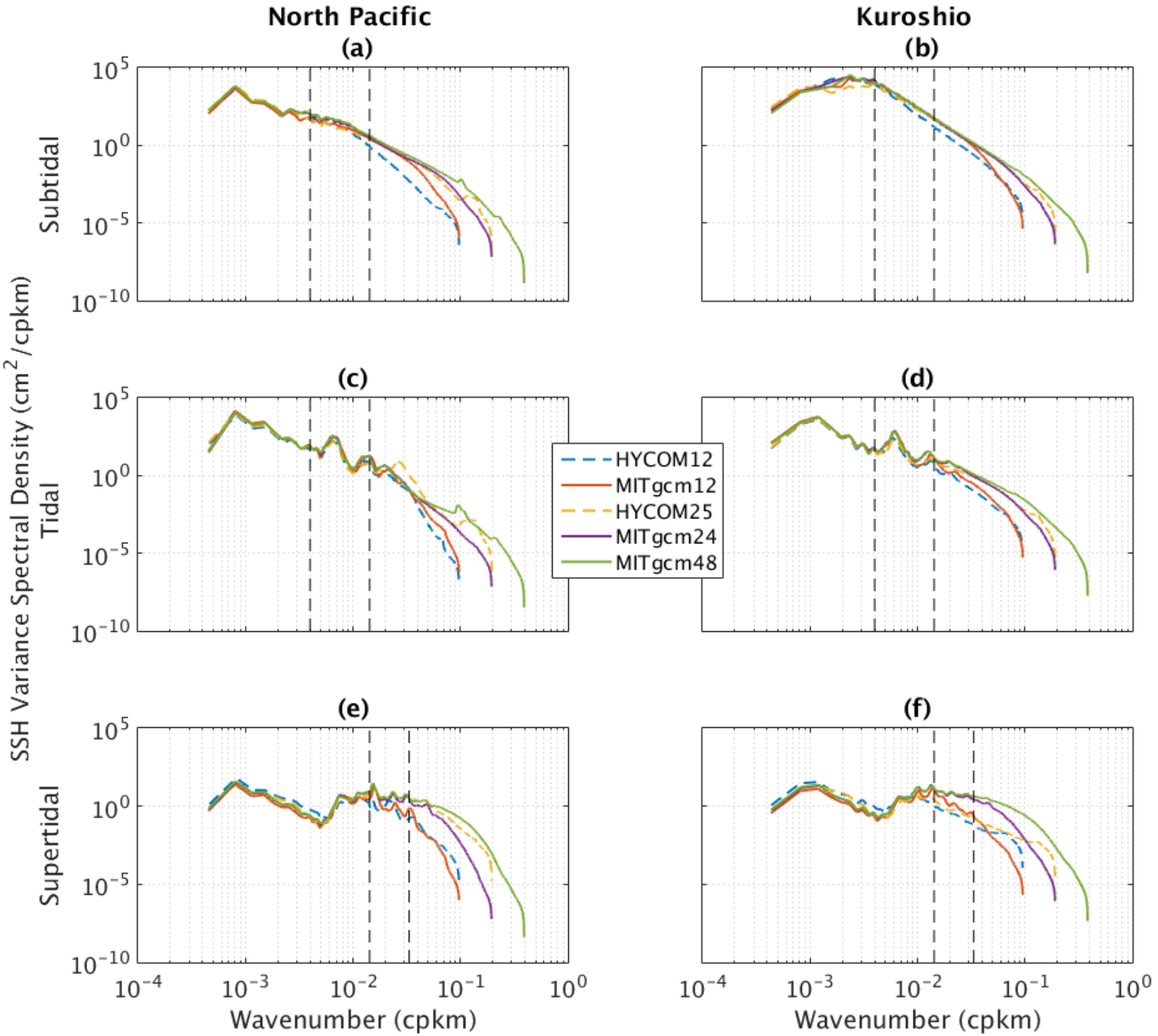

Figure 10.

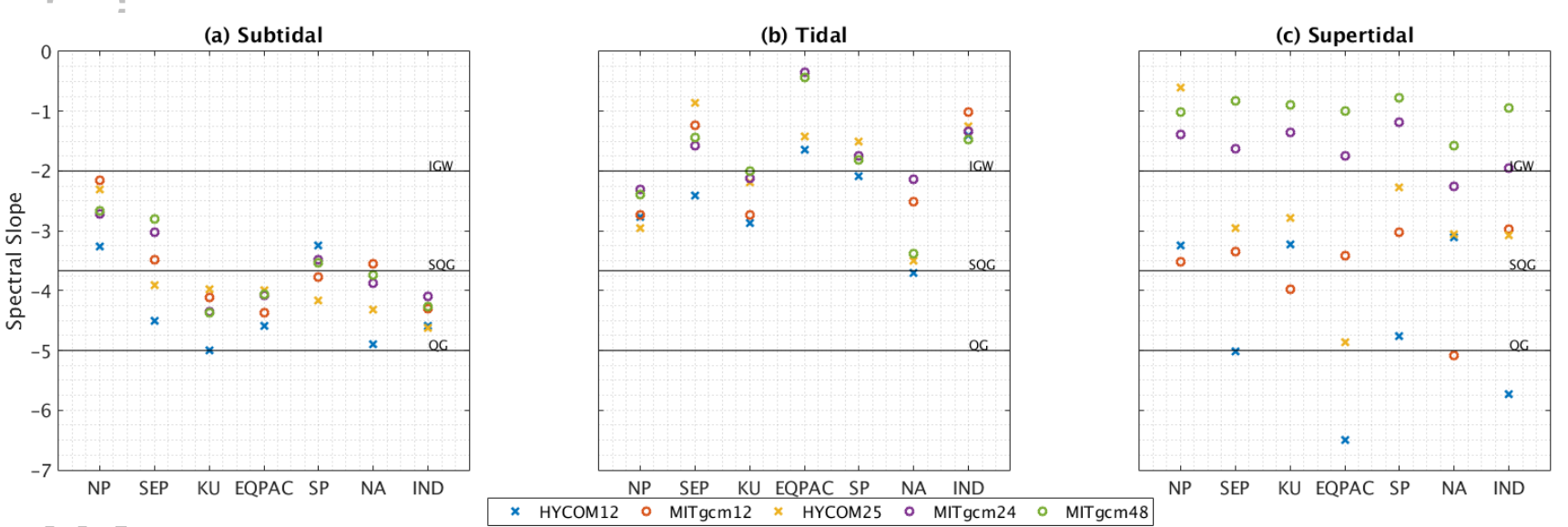
(a) Subtidal
(b) Tidal
(c) Supertidal
Spectral Slope
0
−1
−2
−3
−4
−5
−6
−7
IGW
SQG
QG
NP
SEP
KU
EQPAC
SP
NA
IND
HYCOM12
MITgcm12
HYCOM25
MITgcm24
MITgcm48